
1 This manuscript has been submitted for publication in *Journal of Geophysical Research:*
2 ***Solid Earth***. The peer-reviewed version of this manuscript has been accepted and is in press.
3 The final version of this manuscript will be available via the 'Peer reviewed Publication DOI' link
4 on the right-hand side of this webpage. Please feel free to contact any of the authors; we
5 welcome feedback

6

7 **Title:** Resolving the Kinematics and Moment Release of Early Afterslip within the
8 First Hours following the 2016 M_w 7.1 Kumamoto Earthquake: Implications for
9 the Shallow Slip Deficit and Frictional Behavior of Aseismic Creep

10
11 **Author list:** C., Milliner^{1*}, R., Bürgmann², A., Inbal³, T., Wang⁴, C., Liang⁵

12
13 **Affiliations**

14 ¹ Jet Propulsion Laboratory, California Institute of Technology, Pasadena, CA 91109, USA.

15 ² Department of Earth and Planetary Science, University of California Berkeley, Berkeley, CA 94720, USA.

16 ³ Porter School of the Environment and Earth Sciences, Tel Aviv University, Tel-Aviv University, Ramat-Aviv, Tel-Aviv 69978, Israel.

17 ⁴ School of Earth and Space Sciences, Peking University, China.

18 ⁵ California Institute of Technology, Pasadena, CA 91109, USA.

19
20 *Correspondence to: milliner@caltech.edu

21 **Key Points:**

- 22
- 23 ● The mainshock shows almost no shallow slip deficit, with postseismic cGPS showing
24 minor moment release from early, shallow afterslip.
 - 25 ● Afterslip within the first day is consistent with steady-state velocity strengthening friction
26 showing no delayed nucleation or acceleration
 - 27 ● Afterslip and aftershocks show a close correlation within the first hours following
28 rupture, indicating a possible triggering mechanism.
- 29
30
31

32
33
34
35
36
37
38
39
40
41
42
43
44
45
46
47
48
49
50
51
52
53

Abstract

Continuous measurements of postseismic surface deformation provide insight into variations of the frictional strength of faults and the rheology of the lower crust and upper mantle as stresses following rupture are dissipated. However, due to the difficulty of capturing the earliest phase of afterslip, most analyses have focused on understanding postseismic processes over timescales of weeks-to-years. Here we investigate the kinematics, moment release and frictional properties of the earliest phase of afterslip within the first hours following the 2016 M_w 7.1 Kumamoto earthquake using a network of five-minute sampled continuous GPS stations. Using independent component analysis to filter the GPS data we find that (1) early afterslip contributes only ~1% of total moment release within the first hour, and 8% after 24 hours. This suggests that the slip model of the mainshock, which we estimate using standard geodetic datasets (e.g., InSAR, GPS and pixel offsets), and which span the first four days of the postseismic period, is largely reflective of the dynamic rupture process and we can rule out contamination of moment release by early afterslip. (2) Early afterslip shows no evidence of a delayed nucleation or acceleration phase, where instead fault patches transition to immediate deceleration following rupture that is consistent with frictional relaxation under steady-state conditions with dependence only on the sliding velocity. (3) There is a close correlation between the near-field aftershocks and afterslip within the first hours following rupture, suggesting afterslip may still be an important possible triggering mechanism during the earliest postseismic period.

1. Introduction

54 Analysis from a number of geodetic slip models of large-magnitude continental strike-slip
55 earthquakes have suggested a systematic decrease of coseismic slip in the shallow crust (< 5 km)
56 compared to that at seismogenic depths (~ 6 -10 km), termed the shallow slip deficit (SSD) (Fialko
57 et al., 2005). Numerous mechanisms have been invoked to explain how the rupture may be
58 impeded in the near-surface to produce such slip deficits, including a higher coefficient of fault
59 friction in the shallow crust (Byerlee, 1978), the shallow fault surface having a velocity
60 strengthening frictional rheology (Marone, 1998), interseismic distributed creep or bulk inelastic
61 yielding of the shallow fault-zone that continuously relieves the stored elastic strain (Lindsey et
62 al. 2014), compliant shallow fault zones (Barbot et al., 2008), or dissipation of the rupture energy
63 in the near-surface due to the generation of plastic strain promoted by lower normal stresses
64 (Fielding et al., 2009; Kaneko and Fialko, 2011; Brooks et al. 2017). Knowing how efficiently
65 coseismic ruptures propagate into the near-surface has important implications for accurately
66 simulating the rupture process and generating realistic strong ground motions that affect seismic
67 hazard estimates (Pitarka et al., 2009; Somerville, 2003), as well as how any remnant elastic strain
68 in the shallow crust following a rupture is released throughout the earthquake cycle.

69 A key remaining issue in accurately characterizing the extent of coseismic shallow slip
70 deficits, is that most geodetically constrained slip models contain an unknown amount of
71 postseismic afterslip. Most geodetic imaging data (e.g., InSAR) are acquired within the first days-
72 to-weeks following rupture which makes it challenging to constrain how contaminated current
73 fault slip models are and how biased estimates of the SSD could be from early and possibly rapid
74 afterslip. Recently proposed dual-inversion approaches that jointly solve for both the co- and post-
75 seismic slip with datasets spanning mixed time periods show promise in addressing this issue in
76 the future, but require availability of continuous and high-density datasets and are limited by

77 possible trade-offs (Liu & Xu, 2019; Ragon et al., 2019). Instances where rapid shallow afterslip
78 could be observed include, the 2014 M_w 6.0 Napa earthquake (Lienkaemper et al., 2016) and the
79 2004 M_w 6.0 Parkfield earthquake (Freed, 2007), where measurements were acquired early enough
80 to separate early afterslip from coseismic slip in the shallow crust. For the former, 30-40 cm of
81 surface afterslip was measured after \sim 2 months, which exceeded the coseismic surface slip of \sim 10
82 cm, indicating early postseismic slip can contribute a significant amount to shallow fault slip.
83 Therefore, key questions remain as to what is the contribution of early aseismic afterslip in
84 geodetically constrained slip models and how biased are estimates of shallow slip deficits?
85 Constraining the earliest phase of postseismic relaxation, when rates of aseismic moment release
86 are highest, is therefore necessary to better separate between co- and post-seismic moment release
87 and therefore gain a better understanding of the near-surface pattern of strain accumulation and
88 release.

89 The lack of observational constraints of the early afterslip process (in the hours following
90 rupture), also means the frictional process governing this period is not fully understood. The
91 phenomenological rate-and-state law derived from lab-rock experiments describes how the
92 frictional strength of a fault surface changes as a function of the sliding velocity and state of the
93 surface (Marone, 1998). In the case when the frictional resistance of the fault surface decreases
94 (increases) this leads to unstable (stable) sliding, termed velocity weakening (strengthening)
95 behavior. However, it is not clear how the velocity strengthening sections on natural fault surfaces
96 may respond to stress perturbations in the hours immediately following rupture and whether the
97 relaxation process initially follows a steady or non-steady state regime. Theoretical rate-and-state
98 predictions of afterslip indicate that the difference between a steady and non-steady state behavior
99 can be distinguished by the differences in slip velocity expected within the first few hours

100 following rupture (Perfettini and Avouac, 2007; Perfettini and Ampuero, 2008). Following a stress
101 perturbation imposed by the main rupture, a velocity strengthening patch under steady-state
102 conditions would experience immediate deceleration with the fault strength depending only on the
103 sliding velocity and not also on the state of the surface (i.e., a velocity-strengthening law). While
104 if relaxation initially occurs under non-steady state conditions the fault patch would experience a
105 transient phase of nucleation and acceleration in the first few hours following rupture and exhibit
106 a frictional dependence on both the state and rate variables (i.e., a full rate-and-state law).
107 Therefore, to separate between these two possible frictional behaviors that governs the conditions
108 by which fault patches relax, it is necessary to capture the kinematics of the earliest phase of
109 afterslip. Analysis of high-rate GPS data revealed ~ 1.2 hours following the 2003 M_w 8.0 Tokachi-
110 oki earthquake a possible nucleation and acceleration phase, that was consistent with a sliding
111 behavior dependent upon both the velocity and state of the surface (i.e., non-steady state
112 relaxation) (Fukuda et al., 2009). However, the acceleration phase also coincided with a large
113 aftershock and the interpretation is arguably ambiguous as to whether the sudden change in
114 afterslip rate was due primarily to a delayed response following the main rupture associated with
115 a non-steady state nucleation phase, or simply due to a triggered aftershock (Miyazaki and Larson,
116 2008). An overall lack of observational constraints of the earliest postseismic period makes it
117 difficult to discern whether the frictional process governing afterslip follows a steady-state velocity
118 strengthening behavior or a non-steady state relaxation, limiting our understanding of the frictional
119 conditions that describe aseismic creep.

120 The number of aftershocks following the mainshock are well-known to follow an Omori-
121 like, inverse time decay (Utsu et al., 1995), but there is debate concerning the mechanism(s) behind
122 the aftershock production rate. Numerous studies have found a close correlation between afterslip

123 and the cumulative number of aftershocks (e.g., Frank et al., 2017; Gualandi et al., 2014; Lange et
124 al., 2014; Perfettini and Avouac, 2007), and suggested that afterslip may cause stress changes on
125 locked patches of the fault surface that then triggers aftershocks. Other possible mechanisms
126 include dynamic (Gomberg and Johnson, 2005), or static stress changes from the main rupture,
127 that causes aftershocks on a population of sources (Dieterich, 1994; Toda et al., 2012). Although,
128 there is evidence that near-field aftershocks and afterslip correlate strongly over timescales from
129 days to years following the mainshock, there is still no observational constraints as to whether the
130 afterslip-aftershock relation still holds in the earliest stages following rupture and whether afterslip
131 is still a viable triggering mechanism. To answer these questions, we aim to resolve the kinematics
132 of the earliest afterslip in the first minutes to hours following the 2016 M_w 7.1 Kumamoto
133 earthquake using a network of continuous and relatively high-rate (five-minute sampled) GPS
134 positioning (figure 1). From these observations we seek to test the following questions, (i) Is there
135 significant early and rapid afterslip exist that could bias estimates of shallow coseismic slip deficits
136 derived from geodetic slip models (e.g., figure 2)? (ii) What is the frictional process governing the
137 early postseismic phase? and (iii) Does the afterslip-aftershock relation also hold in the hours
138 following rupture?

139 The 2016 M_w 7.1 Kumamoto earthquake occurred within a dense network of
140 Japan's continuous GNSS stations (GEONet) (Sagiya et al., 2010), and provides a unique
141 opportunity to capture the temporal evolution of early afterslip within the first minutes following
142 the mainshock rupture. In our analysis we first derive a mainshock slip model for the oblique
143 strike-slip rupture that is estimated from jointly inverting ascending and descending InSAR, GPS,
144 and radar pixel offsets that bracket the mainshock, and like most geodetically constrained slip
145 models contains a component of early postseismic deformation. To then reliably detect the early

146 afterslip signal from the noisy five-minute sampled GPS data we use independent component
147 analysis (ICA), a spatiotemporal filtering technique to extract the dissipating tectonic signal
148 (Hyvärinen and Oja, 2000). An advantage of the ICA approach is that it can separate the afterslip
149 signal from systematic and local noise sources on the basis of statistical independence, obviating
150 a need to impose an assumed functional form as to how the GPS velocities and the inverted
151 afterslip should evolve (such as a log-time or exponential model). We then invert the filtered GPS
152 time series to generate an ‘early’ afterslip model (spanning the first six days following rupture),
153 constrained using five-minute sampled GPS positioning, and a ‘longer-term’ afterslip model
154 derived from daily GPS positioning over the first two years (Kositsky and Avouac, 2010). From
155 the ‘early’ and ‘longer-term’ afterslip models we can assess the contribution of afterslip to moment
156 release in the shallow crust and the extent to which it may contaminate the geodetically constrained
157 mainshock slip model and estimates of any possible coseismic slip deficits. Using the early afterslip
158 model over the first six days, we then attempt to distinguish what frictional regime (steady or non-
159 steady state) is compatible with the temporal evolution of afterslip. Finally, comparing the
160 evolution of nearfield aftershocks, derived from a template-matching catalogue, to early afterslip
161 from our GPS inversion, we can then assess whether the afterslip-aftershock relation, that has been
162 widely observed at daily-annual timescales, still holds within the hours following rupture.

163

164 **1.2 Tectonic setting**

165 The 2016 M_w 7.1 Kumamoto earthquake ruptured along the Median Tectonic Line, a major
166 NE-trending fault system that is part of a transtensional backarc setting accommodating oblique
167 Eurasian-Philippine collision (Figure 1), (Ikeda et al., 2009). The 2016 M_w 7.1 event involved two
168 main fault segments, the NNE-striking Hinagu fault which ruptured for ~ 10 km, which was the

169 site of rupture initiation and also hosted one of two $M_w \geq 6$ foreshocks, and the NE-striking
170 Futugawa fault to the northeast, that ruptured for ~ 25 km and where the rupture terminated within
171 the Aso volcano (Shirahama et al., 2016).

172 Analysis of postseismic deformation following the 2016 Kumamoto earthquake has focused
173 on resolving the deep viscoelastic relaxation response of the lower crust and upper mantle. Moore
174 et al. (2017) developed Green's functions to invert crustal strain rates to estimate the transient
175 lower-crustal rheology below 20 km depth, finding effective viscosities as low as 5×10^{16} Pa.s
176 near the Aso volcano. Similar low transient viscosities of $\sim 10^{17}$ Pa.s were also found by Pollitz et
177 al. (2017) below 20 km along the central graben system through Kyushu island, which suggested
178 a fluid-rich mantle wedge above the Nankai trough. Compared to these longer-term and deeper
179 crustal studies of postseismic relaxation, here we focus on understanding the aseismic afterslip
180 process within the shallow crust (top 10 km) and first few hours following rupture.

181

182 **2. Data**

183

184 To determine the coseismic and postseismic slip distributions we used a range of geodetic data
185 including SAR offsets, InSAR, and continuous GPS, (figure 3).

186

187 **2.1 InSAR**

188

189 To measure the far-field coseismic surface deformation, we processed Sentinel-1 ascending
190 (Track 156) and descending (Track 163) pairs acquired in Terrain Observation by Progressive
191 Scan (TOPS) mode following standard two-pass interferometry procedures. The preseismic and

192 postseismic images were acquired on 8 April and 20 April 2016, respectively (Tabls S1). To
193 remove the topographic phase from the SAR images we used a 1-arcsecond SRTM (Shuttle Radar
194 Topography Mission) DEM, and unwrapped the images using the Statistical-Cost Network-Flow
195 Algorithm for Phase Unwrapping (SNAPHU) algorithm (Chen and Zebker, 2001). The unwrapped
196 phase was then downsampled using a quadtree algorithm (figure 3 a, b). Near-field displacements
197 were estimated using split-bandwidth interferometry along the range direction and burst-overlap
198 interferometry along the azimuth direction, respectively following the method of Jiang et al. (2017)
199 (Figure 3 g, h). We also processed a single descending ALOS-2 interferogram that spanned the
200 M_w 6.0 and M_w 6.2 foreshocks (Fig. S1 and Table S1), that occurred \sim 19 and \sim 15 hours before the
201 mainshock, respectively, which we inverted to estimate a foreshock slip model and correct for its
202 effect in the geodetic data that brackets the M_w 7.1 mainshock.

203

204 **2.2 3D near-field measurements**

205

206 To measure the near-field coseismic surface deformation in areas where the unwrapped radar
207 phase decorrelates as a result of large surface changes (figure 3 d-f), we used cross-correlation of
208 ALOS-2 SAR data in both the range and azimuth directions (Liang and Fielding, 2017). Deriving
209 offsets in the range and azimuth direction from a total of three image pairs (two from descending
210 and one from ascending tracks, see Table S1), provides six unique look directions of surface
211 deformation at decimeter-level precision and \sim 25 m ground resolution. From the six look
212 directions we solved for the three-dimensional surface motions (east u_e , north u_n and up u_u), using
213 a weighted least-squares approach (see eq. 1 and 2, and Figure 3 d-f for results, Fialko et al., 2001).

214

215

$$\mathbf{P} = \begin{bmatrix} p_{azi}^{desc-l} \\ p_R^{desc-l} \\ p_{azi}^{desc-r} \\ p_R^{desc-r} \\ p_{azi}^{asc-r} \\ p_R^{asc-r} \end{bmatrix} \quad (1)$$

216

$$[u_e \ u_n \ u_u] = (\mathbf{P}^T \Sigma_d \mathbf{P})^{-1} \mathbf{P}^T d \quad (2)$$

217

218 Where p is the unit vector representing surface motion projected into the range (R) or along-
 219 track (azi) direction, where the superscript in eq. (1) denotes whether the satellite was in an
 220 ascending (asc) or descending (desc) orbit and looking left (l) or right (r). The diagonal
 221 components of the weighting matrix (Σ_d) includes the inverse of the variance estimated from a far-
 222 field stable region, and d is the data vector containing the offset values. From the 3D deformation
 223 maps we then extracted the horizontal and vertical fault slip offsets along the surface rupture using
 224 stacked profiles oriented perpendicular to the fault traces, which produces the along-strike surface
 225 slip distribution (Figure 3i). These offset measurements provide an estimate of the total surface
 226 displacement across the entire rupture-zone width (i.e., both the on and off-fault deformation), by
 227 extrapolating the surface motion from either side of the fault zone towards the primary fault trace
 228 (e.g., Rockwell et al., 2002; Milliner et al., 2015). The surface slip distribution shows a slightly
 229 asymmetric elliptical shape with a sample mean displacement of 2.36 ± 0.4 m (standard error), and
 230 a maximum of 2.86 ± 0.67 (1σ) m located northeast of the Hinagu-Futugawa fault intersection,
 231 and have good agreement with offsets estimated from 2D subpixel correlation of a pair of Sentinel-
 232 2 optical images processed using COSI-Corr (Figure S2) (Leprince et al., 2007). These near-field
 233 ALOS-2 offset measurements help constrain fault slip in the top cells of the slip model and are

234 therefore complementary to the other geodetic observations used here (e.g., InSAR and GPS),
235 which constrain the far-field elastic response of the crust due to deeper slip.

236

237

238 **2.3 GPS**

239 For both the coseismic and postseismic slip models we used 63 continuous GPS stations.

240 For the early phase of afterslip (during the first six days), we used the five-minute sampled time

241 series, and to study the longer-term postseismic process (the following two-years) we used the

242 daily sampled product. The GPS time series were obtained from the Univ. of Nevada Reno

243 geodetic lab (<http://geodesy.unr.edu/>), (Blewitt et al., 2018), which processes the time series in

244 precise point positioning mode using GIPSY/OASIS-II version 6.1.1. The time series are aligned

245 to the IGS08 reference frame, and have been corrected for diurnal, semidiurnal, M_f , and M_m ocean

246 tide loading using the tidal model FES04, while the semi-annual tidal loading as well as the solid

247 Earth tide and pole tide have been corrected following the IERS (International Earth Rotation and

248 Reference Systems Service) 2010 conventions (Petit and Luzum, 2010). The Earth Orientation

249 Parameters of the model have been calculated using the IERS 2010 conventions for diurnal, semi-

250 diurnal, and long period tidal effects. To estimate the coseismic offset at each station we used the

251 five-minute sampled time series, and removed a pre-earthquake velocity using positions six days

252 prior to the mainshock and then simply differenced the average position in all three components

253 from one hour before and after the event (figure 3c). For the postseismic GPS analysis we describe

254 in the next section the use of a spatio-temporal filtering technique to help extract the time-varying

255 afterslip signal and to improve the signal-to-noise ratio.

256

257 **3. Methods**

258

259 **3.1 Spatiotemporal filtering using Independent Component Analysis (ICA)**

260

261 One of the major noise sources in the analysis of regional GPS networks is common-mode
262 error (CME). This systematic noise source is thought to arise from a combination of uncertainties
263 in GPS orbital position, reference frame and large-scale atmospheric modeling (Dong et al., 2006;
264 Serpelloni et al., 2013; Wdowinski et al., 1997; Williams Simon D. P. et al., 2004). To isolate and
265 separate the tectonic signal from systematic noise sources such as CME, we use a spatiotemporal
266 filtering technique called ICA (Le et al., 2011). ICA is a form of blind source separation that seeks
267 to separate a set of latent variables under the assumption that they are statistically independent (see
268 section S1 for more details on the ICA method). Here, we have used the reconstruction ICA
269 approach (Le et al., 2011) to estimate the unknown sources, which differs from other ICA methods,
270 such as fastICA (Hyvärinen and Oja, 2000), by swapping the orthonormality constraint applied to
271 the un-mixing matrix, with a reconstruction penalty term added explicitly to the objective function,
272 which gives the benefit of using unconstrained solvers (see equation 2 of Le et al. (2011), and
273 section S1 and eq. S1 here). The ICA approach allows for a variable spatial weight for each station
274 and source, allowing ICA to account for correlated, spatially varying CME across the network
275 (Dong et al., 2006), which is advantageous over typical network filtering techniques such as
276 regional stacking, which assumes regional stacking is a uniform effect (Wdowinski et al., 1997).
277 To determine the number of components to decompose the data into, we used North's rule of
278 thumb (North et al., 1982), a stopping-rule approach that helps define the statistical significance
279 of each component relative to its uncertainty (see section S2 for additional details). For the five-

280 minute GPS data, we found that four components were significant, and for the daily GPS data, five
281 components (Figure S7).

282 The ICA filtering is applied separately to the five-minute and daily GPS time series, giving
283 independent constraints of the early and later phases of postseismic surface deformation. For the
284 five-minute time series we were not able to include the vertical component, as we could not resolve
285 a robust tectonic signal due to the large noise. However, for the daily longer-term time series we
286 were able to use all three-components of motion. From the ICA decomposition of the five-minute
287 sampled, early postseismic GPS data (figure 4), we interpret the first and second ICs as
288 representing CME due to the uniform spatial response, incoherent temporal pattern and the largest
289 contribution to variance (eq. S2). We interpret the fourth IC as the tectonic signal (figure 4), as it
290 exhibits a temporal component with a clear log-like time decay and a spatial response that is
291 consistent with fault-related shear motion across the north-east trending Kumamoto rupture.
292 Projecting the data onto this single component reduces the WRMS by 91% (the median value
293 estimated from all stations). We suspect that the third component is related to either volcanic and/or
294 non-tidal ocean loading (or both) due to the large spatial responses in proximity to the active
295 volcanoes (black triangles in Figure 4d) and coastal regions. For the longer-term postseismic, daily
296 time series, we find that the second, third and fourth ICs reflect periodic signals and CME, while
297 the tectonic signal is represented by the first IC (Figure S4). Selecting only the first IC reduces the
298 WRMS of the time series on average by 47%, a smaller decrease than that found from the five-
299 minute data because the long-term postseismic signal still contributes a relatively larger amount
300 of the total variance of motion across the network.

301 In postseismic studies that use daily sampled GPS positioning, typically the first
302 postseismic day is defined as the reference epoch from which future changes in position are

303 measured from. However, this step removes any post-seismic motion that may have accrued within
304 the first day following rupture, which can contribute a significant amount of displacement (Hill et
305 al., 2012; Twardzik et al., 2019). Here, as we can measure the total displacement of each station
306 within the first 24 hours after the earthquake using the higher rate (5-minute) sampled positioning
307 (figure 6), we correct the daily postseismic GPS positions to include this amount by taking the
308 average amount of displacement measured within the first 24 hours (of the first postseismic UTC
309 day, which is ~8 hours after the event and includes motion up to this time). This increases the daily
310 GPS displacement by up to 14 mm for some near-field stations (Fig. S20).

311

312 **3.2 Inversion of Geodetic Data for fault slip**

313 To estimate the coseismic slip distribution we invert the geodetic data (Fig. 3), using a
314 weighted non-negative least-squares method assuming a homogenous elastic half-space (Okada et
315 al., 1992), and apply a finite-difference gradient smoothing regularization to the solution. The
316 time-varying postseismic slip is estimated using an inversion approach similar to the independent
317 component analysis-based inversion method (ICAIM) (Kositsky and Avouac, 2010), using only
318 the GPS time series, and where we deepen, lengthen and coarsen the fault segments. To estimate
319 the fit of both the co- and postseismic models to the data and variations in the degree of smoothing
320 we use the percent of variance reduction (POVR) (see eq. S3, and section S7 and for more details
321 of the inversion approach and fault parameterization).

322

323 **4. Results**

324 The mainshock slip model is able to fit the geodetic data well, with POVR values of 91%
325 for the GPS, 97% for the ALOS-2 radar fault offsets, 89% for the Sentinel-1A azimuthal offsets,

326 93% for the Sentinel-1 range offsets, 63% for the descending InSAR, and 86% for the ascending
327 InSAR (see Figure S3 for fits and residuals). The relatively poor model fit to the descending InSAR
328 data is likely the result of the inability of the elastic model to reproduce the complex non-tectonic
329 deformation within the Aso caldera that resulted from lateral spreads and shaking-induced
330 slumping, where we find the largest misfits (Fig. S3), (Tajima et al., 2017; Tsuji et al., 2017).

331 The mainshock slip model indicates a total seismic moment of 3.86×10^{19} N·m, that is
332 equivalent to a moment magnitude of $M_w = 7.06$ (assuming a shear modulus of 30 GPa), that is
333 close to the seismologic estimate from strong ground motion inversion of $M_w = 7.06$ (3.9×10^{19}
334 N·m) Hao et al. (2016), and the USGS GCMT of $M_w = 7.0$. Largest slip of 5.48 ± 0.3 m is found
335 along the Futugawa fault at ~ 9 km depth that decreases sharply along-strike to zero towards the
336 Aso volcano, a feature common amongst other coseismic models derived from geodetic and
337 seismologic data (Asano and Iwata, 2016; Yagi et al., 2016; Kobayashi et al., 2017; Scott et al.,
338 2019), and large shallow slip along the south-west end of the Futugawa fault (2-3 m), also
339 consistent with previous slip models (see Figure S14).

340

341 **4.1 Early postseismic afterslip**

342

343 To resolve the kinematics and moment release of the earliest phase of afterslip in the first hours
344 following rupture we inverted the filtered GPS five-minute sampled time series over the first six
345 days. The kinematic afterslip model shows a reasonably good fit to the GPS time series, with
346 POVR of 85% and 88% for the east, and north components, respectively. The afterslip moment
347 decays almost in a log-time fashion, as illustrated in figure 7c. After the first hour the total
348 cumulative aseismic moment amounts to 3×10^{17} N·m ($M_w = 5.7$), which is $\sim 1\%$ of seismologic

349 coseismic moment, and after 24 hours is 3×10^{18} N·m ($M_w = 6.3$), or 8% of the coseismic moment
350 release (Hao et al., 2016). Within the top 5 km of the crust we find that the moment release from
351 afterslip is almost half of the total aseismic moment (or 4% of the coseismic amount), with only
352 1.5×10^{17} N·m released within the first hour and 1.5×10^{18} N·m after 24 hours. Afterslip on the
353 Futugawa fault is almost zero within the main area of large coseismic slip at ~ 10 km depth,
354 suggesting our afterslip model can resolve the first-order features of the slip distribution (see also
355 figure S10 for model uncertainty estimates).

356

357 **4.2 Longer term afterslip**

358

359 To constrain the longer-term moment release from afterslip and its contribution to
360 compensating for deficits in shallow coseismic slip, we inverted the daily ICA filtered GPS time
361 series over the first two years following the mainshock. Aseismic moment release again exhibits a
362 log decay with time, where after two years we find a total aseismic moment of 1.2×10^{19} N·m,
363 that is $\sim 30\%$ of the seismologically estimated moment (Asano and Iwata, 2016), and within the
364 top 5 km of the crust an aseismic moment of 5.1×10^{18} N·m, or $\sim 13\%$ compared to the coseismic
365 amount. Within regions of the model space that we can resolve well (< 20 km depth, Figure S10)
366 the spatial distribution of longer-term afterslip shows a similar spatial pattern to the early afterslip
367 (Figure 7). Over the first two years there is again a noticeable lack of afterslip within the main
368 coseismic asperity patch on the Futugawa fault and immediately below the Aso volcano at depth
369 (< 20 km).

370

371 **4.3 Deficits of Shallow Co- and Postseismic Slip**

372

373 To characterize how co- and post-seismic slip varies as a function of depth and any possible
374 shallow slip deficits, we integrate the norm of the slip vector along-strike for each depth layer and
375 normalize by the largest value (Figure 5b). This is calculated across both the Hinagu and Futugawa
376 faults, giving the average slip-depth distribution across the entire rupture plane. The SSD value is
377 then estimated from the normalized slip-depth function in Figure 5b as, $[1 - (S_s/S_{max})] \cdot 100$, where
378 S_s is the integrated surface slip value and S_{max} is the maximum integrated slip at any depth. The
379 slip-depth distribution from the mainshock model (which includes early afterslip, figure 5) exhibits
380 almost no deficit, at $2 \pm 3\%$, indicating that the overall surface slip across the rupture plane is
381 similar to that at depth (Figure 5b). However, in local areas of the rupture the slip-depth distribution
382 can be found to significantly deviate from this rupture-average slip deficit. For example, along the
383 mid-section of the Futugawa fault where the main slip asperity is located, there is locally a large
384 SSD of $33 \pm 6\%$. Whereas further to the southwest along the Futugawa fault there is interestingly
385 a site of higher slip at the surface (1.87 m) than that at depth (1.1 m) producing a negative SSD ($-$
386 $50 \pm 8\%$), which we term a shallow slip surfeit (SSS). This surfeit can explain why the rupture-
387 averaged SSD is close to zero and that the overall slip is balanced across the rupture plane. We
388 note that other slip models estimated using different datasets (strong ground motion data and
389 InSAR), show a similar SSS along the southwest end of the Futugawa fault (see Figure S14),
390 (Asano and Iwata, 2016; Jiang et al., 2017; Kobayashi et al., 2017; Yagi et al., 2016).

391 Reliable estimates of the slip-depth distribution require near-field geodetic observations of
392 surface deformation to help constrain slip at shallow depths (< 5 km) (Xu et al., 2016) as well as
393 consideration of the effects of the spatial smoothing associated with regularization of the solution.
394 Here we incorporate 3D ALOS-2 SAR offsets and Sentinel-1 range offset data into the inversion

395 that we find provides reasonable constraints for shallow slip as found by low model uncertainty
396 estimates of < 15 cm (figure S9) and high model resolution values of > 0.9 at depths < 5 km (Figure
397 S8, Du et al., 1992). To mitigate the effects of spatial smoothing, which can problematically flatten
398 the slip-depth distribution and underestimate the slip deficit, we use a similar approach of Xu et
399 al. (2016) where a minimal smoothing factor is chosen that corresponds to the start of the decrease
400 in model fit measured using the POVR (Fig. S17). This approach is advantageous over a typical
401 L-curve method as the optimal trade-off location (point of maximum curvature) between the model
402 misfit and roughness is arbitrarily dependent upon the range of values chosen (Hreinsdottir et al.,
403 2002).

404

405 **4.4 Frictional analysis**

406

407 To constrain the frictional behavior of the fault surface undergoing afterslip (i.e., a - b ,
408 which controls the instantaneous (a) and the steady-state velocity-dependence of friction (b)) we
409 use a simple velocity-strengthening friction sliding law (Marone, 1998; Dieterich, 2007). The
410 velocity strengthening law models the evolution of afterslip as a zero-dimensional spring-block
411 slider system responding to an imposed stress change, with dependence only on the rate and not
412 on the state variable, an assumption that we discuss and justify later in section 5.3 where we find
413 that the kinematics of the observed afterslip are inconsistent with a full rate-and-state law. The
414 frictional parameters (a - b) are estimated by fitting the time evolution of afterslip, $\delta(t)$, of the
415 velocity strengthening model shown in eq. (3) to model fault patches that experience an increase
416 of Coulomb stress. The velocity strengthening law models the evolution of afterslip relative to a
417 reference epoch (t_l), chosen here as the first sample five-minutes after the mainshock (following

418 Gualandi et al., 2014),

419

$$420 \quad \delta(t) - \delta(t_1) \approx \alpha \ln\left(\frac{\alpha + \beta t}{\alpha + \beta t_1}\right) \quad (3)$$

421

422 with the assumption that the period of observation t is smaller than the characteristic decay time

423 ($t_d = \alpha / V_{pl}$), where V_{pl} = loading plate velocity. From Marone et al. (1991), $\alpha = (a-b) \sigma / k$ and β

424 is the starting sliding velocity on the patch at the onset of postseismic slip ($t \approx 0$), σ the effective

425 normal stress on the fault surface and k is the spring stiffness representing the rigidity of the host

426 rock. We assume an effective normal stress (lithostatic-hydrostatic pressure, with density of 2700

427 and 1000 kg/m³, respectively), $k = 30$ GPa, and $V_{pl} = 2$ mm/yr derived from paleoseismic analysis

428 of the Futugawa fault (Lin et al., 2017). From eq. (3) we estimate α and β for the early phase of

429 afterslip from each fault patch using a non-linear inversion method, finding values from 0.1-1.5

430 cm and 0.1-2.5 cm/hour, respectively. This indicates a t_d of ~ 5.6 years, which is significantly larger

431 than the GPS observation period of six days, indicating that the condition $t \ll t_d$ in eq. (3) is

432 satisfied. Coulomb stress changes (ΔCFF) are then calculated for each afterslip patch using the

433 stress changes due to the mainshock slip model (figure 5), and assuming a static frictional

434 coefficient of $\mu_s = 0.4$. Using the estimate of β derived from the early phase of afterslip and eq. 4

435 we find $a-b$ values along the Hinagu and Futugawa faults ranging from 10^{-4} - 10^{-2} (Figure 8). We

436 do not apply the frictional analysis to afterslip estimated over the longer-term (two years), because

437 this later phase of deformation is increasingly affected by viscoelastic relaxation which we do not

438 formally correct for.

$$439 \quad a - b = \frac{\Delta CFF}{\sigma \cdot \log\left(\frac{\beta}{V_{pl}}\right)} \quad (4)$$

440

441 Estimates of β also provide constraint for the time of maximum slip velocity (Perfettini &
442 Ampuero, 2008), which we find ranges from ~3 hours-140 days, indicating the temporal sampling
443 of the GPS data (5-minutes) and period of observation (up to 2 years) should be sufficient to
444 resolve the possible occurrence of a transient phase of acceleration (see section S6 for details).

445

446 **5. Discussion**

447

448 **5.1 Shallow slip deficits**

449

450 A remaining problem in understanding the true extent of the shallow slip deficits for large
451 magnitude earthquakes, is the extent of contamination of geodetically constrained slip models by
452 early and possibly rapid afterslip. Such mixing of co- and early postseismic slip in finite-fault
453 models is problematic as it would bias our understanding of the rupture kinematics, such as how
454 well the rupture propagates through the near-surface and how the accumulated elastic strain in the
455 shallow crust that may not be fully released coseismically, is relieved later on in the earthquake
456 cycle (assuming strain is conserved with depth over time). Inversion of the five-minute sampled
457 GPS positioning reveals that the slip-depth distribution of early afterslip resolved after the first
458 day shows it is mostly concentrated in the upper 5 km of the crust (Figure 7a). The largest
459 concentration of early afterslip (up to 15 cm) occurs near the Hinagu and Futugawa fault
460 intersection and along the Futugawa fault, with smaller amounts above and northeast of the large
461 main slip patch, which is consistent with aseismic slip acting to relax strains imposed in the shallow
462 crust. Importantly this shows in this case that even in regions where there are large local coseismic

463 slip deficits, early and rapid afterslip does not compensate significantly for such coseismic deficits
464 in the shallow crust. Overall, the total early afterslip after the first hour following rupture, amounts
465 to only $\sim 1\%$ of moment release by the mainshock, and 8% by the end of the first day, with 4%
466 released in the upper 5 km of the crust (where the coseismic moment is constrained from
467 seismology and independent of aseismic afterslip), and maximum postseismic slip of $\sim 24 \pm 8$ cm.
468 This indicates that for the Kumamoto earthquake, rapid and early afterslip does not contribute a
469 significant amount of slip in the shallow crust. In addition, it suggests that the balanced slip-depth
470 distribution from the mainshock slip model (an SSD of almost zero), is largely reflective of the
471 dynamic rupture process. The relatively low amount of afterslip for this event may indicate that
472 relatively larger shallow afterslip found in other earthquakes (e.g., the 2014 Napa and 2004
473 Parkfield earthquakes), may only pertain to smaller magnitude events ($M_w < 6.5$), which are
474 ruptures that fail to completely propagate through the surface. This behavior was noted by Fattahi
475 et al. (2015), that found from a compilation of 22 events, that more moderate earthquakes ($M_w <$
476 6) have a larger relative amount of shallow postseismic slip than coseismic. A possible reason for
477 this difference in behavior is that smaller events typically occur on less structurally well-developed
478 faults with a rougher geometry, or the effects of velocity strengthening friction in the shallow crust,
479 which can both inhibit efficient rupture within the near-surface and lead to incomplete stress drops
480 (Ma, 2008).

481 To understand whether the near-zero slip deficit we find is a robust feature we compare it
482 against estimates from other slip models of the Kumamoto earthquake inverted using different
483 datasets and inversion strategies (figure 5b) (Asano and Iwata, 2016; Yagi et al., 2016; Kobayashi
484 et al., 2017; Scott et al., 2019). Although there is a range of behaviors for how coseismic slip varies
485 with depth, most indicate slip at the surface is similar to that at seismogenic depths (6-8 km), with

486 SSD values ranging from 1-15%. The model with the largest slip deficit of ~15% is that of Scott
487 et al. (2019), which uses similar geodetic data as that used here (including Sentinel-1 InSAR to
488 constrain far-field deformation and near-field constraints from optical image correlation and lidar
489 data). However, two differences between these studies is that here we have incorporated 3D near-
490 field offsets along the entire length of the surface rupture (~35 km) as opposed to only ~14 km
491 constrained by the lidar data, and the other is the manner in which the near-field data are inverted.
492 Regarding the latter, instead of inverting the measurements of surface motion directly (e.g., Fig. 3
493 d-f), which would assume all near-field motion is elastic, we have instead inverted the fault offsets
494 (Fig. 3i), which approximates the full fault-zone ‘displacement’ as being a combination of the
495 discrete (traditional on-fault displacement) and distributed fault-parallel inelastic shear, the latter
496 which cannot be modeled elastically (Gold et al., 2015; Milliner et al., 2015; Fujiwara et al., 2016;
497 Shirahama et al., 2016; Toda et al., 2016). This explicitly constrains the top cells of the model
498 using the total across-fault inelastic ‘strain’ (e.g., Xu et al. 2016), which includes the distributed
499 component of inelastic shear strain that is known from geologic and geodetic observations to
500 accommodate a significant portion (up to 40%) of the total coseismic fault strain (Rockwell et al.
501 2002; Dolan & Haravitch, 2014; Zinke et al., 2014; Gold et al. 2015; Milliner et al. 2015, 2016;
502 Teran et al. 2015; Scott et al., 2018). We note that the 15% SSD value reported here for the Scott
503 et al. (2019) study differs from their reported value as we have found their approach to calculate
504 the slip-deficit (which uses the median value for each depth interval) leads to a slight
505 underestimation of shallow slip (see supplements section S3 for more details), and is a different
506 approach to that used by previous work and here (which integrates the total slip for each depth
507 interval, e.g., Fialko et al., 2005; Xu et al., 2016). Although, there are differences in the extent of
508 the SSD and slip-depth functions between the various slip models (figure 5b), such variation is

509 useful in characterizing the epistemic uncertainty of the slip-depth distribution and SSD estimates,
510 which arises from the use of different parameterizations, types of regularization (here we minimize
511 the gradient, while others use a curvature penalty), strength of smoothing, data weighting, and data
512 types. The first-order agreement of the slip-depth functions between the various slip models
513 (Figure 5b), and the use of 3D near-field data here to constrain shallow slip, gives us confidence
514 that the coseismic shallow slip of the Kumamoto earthquake is likely similar to that at seismogenic
515 depths. In addition, as our postseismic GPS analysis indicates there is minimal contamination from
516 early afterslip, this supports the notion that the balanced slip distribution found from the mainshock
517 model (i.e., lack of shallow slip deficit), can be regarded as a feature reflective of the dynamic
518 rupture process (e.g., Fig. 2b).

519 Decomposing the overall ‘oblique’ slip-depth distribution, which has almost no deficit
520 (~2%, Fig. 5b), into the dip-slip and strike-slip components shows a prominent surfeit and minor
521 deficit (~10%), respectively (Fig S22). If it is assumed that over multiple earthquake cycles strain
522 release is conserved with depth, these large differences in the co-seismic slip-depth distributions
523 raise the question as to how it is accommodated over the longer-term? Specifically, what is not
524 understood is whether these coseismic slip surfeits and deficits are a persistent feature, or if the
525 slip vector may change considerably from event-to-event that may eradicate slip deficits from prior
526 events and conserve the long-term slip budget. Evidence of considerable variation in the slip vector
527 from event-to-event has been found (by up to almost 90°) from geologic observations of
528 slickenlines, fibre lineations and gouge fabrics from other fault systems (e.g., the Makran fault
529 system, Platt et al., 1988). On the other hand, if the coseismic slip-depth distributions are persistent
530 and reflective of the longer-term strain release, this would suggest that the depth distribution of
531 interseismic release of elastic strain (e.g., via distributed bulk inelastic yielding), must be different

532 in order to conserve the long-term slip budget with depth. Understanding the persistence or lack
533 thereof, of slip deficits and surfeits from event-to-event has important implications for
534 understanding the evolution of strain and stress in the crust, interpreting the incomplete record of
535 paleo-earthquake slip, and realistic dynamic rupture simulations and calculations of seismic
536 shaking for accurately characterizing the hazard.

537 We note that another possible mechanism to explain the lack of a slip deficit for this rupture
538 is the presence of the Aso volcano at the north-east termination of the rupture. This is a region of
539 elevated crustal temperatures which would inhibit slip at depth and limit slip to the shallow surface.
540 This would produce a pronounced shallow slip surfeit in this region which would act to lower the
541 overall slip deficit when considering the slip variation along the entire rupture length.

542

543 **5.2 Aftershock-Afterslip relation**

544 To assess whether a relation exists between the rate of aftershocks and afterslip in the early
545 stages of postseismic relaxation, we compare our early afterslip model to aftershocks from a
546 seismic catalogue from Yue et al. (2017). Such a correlation has been interpreted as the afterslip
547 process influencing the aftershock production, due to afterslip loading unstable patches of the fault
548 surface that then break in aftershocks. To help expand the number of aftershock events we use a
549 seismic catalogue generated using a template matching approach (Ross et al., 2016; Shelly et al.,
550 2016), leading to 35,703 precisely located aftershocks (see Yue et al., 2017 for details).
551 Comparison of the evolution of the cumulative number of aftershocks (using only well-detected
552 events of $M_w > 2$) with early afterslip shows that within the first six days they both follow a similar
553 temporal decay. A similar afterslip-aftershock relation has been observed elsewhere following
554 other large events such as the 1992 Landers, 2009 L'Aquila, 2010 Maule and 2015 Illapel

555 earthquakes (Frank et al., 2017; Gualandi et al., 2014; Lange et al., 2014; Perfettini and Avouac,
556 2007), but has only been observed in the later stages of the aftershock sequence, at timescales of
557 days-years following the mainshock. Here we show that this relation still holds within the first
558 hours following the main event over the first six days (Figure 7c), suggesting afterslip may still
559 influence and possibly trigger aftershocks even at these early timescales, alongside the effects of
560 dynamic and static Coulomb stresses (Dieterich, 1994; Gomberg and Johnson, 2005).

561

562 When comparing the longer-term decay of aftershocks with afterslip (Figure 7d) over the
563 first two years, we find a noticeably weaker correlation. We interpret the afterslip-aftershock
564 discrepancy as the result of an increasing contribution of viscoelastic relaxation to the surface
565 deformation field, that is known to have a larger effect over longer timescales of months-years
566 (Freed et al., 2006) and has not been removed from the daily GPS time series. A prominent
567 viscoelastic response is not surprising given previous postseismic geodetic studies over the first
568 nine months following the Kumamoto earthquake found transient weak viscosities of 10^{17} - 10^{18}
569 Pa·s that are likely related to arc-magmatism (Moore et al., 2017; Pollitz et al., 2017). A prominent
570 viscoelastic response would also explain why the GPS time series exhibits a slower decay rate than
571 the aftershock rate (Figure 7d), and why our afterslip model exhibits a relatively poorer fit to the
572 vertical component of the GPS data than the horizontals (POVR of 67% and 83%, respectively,
573 see Fig. S18). This apparent afterslip-aftershock discrepancy contrasts with other earthquakes,
574 such as following the 2004 Parkfield or 1992 Landers events, which showed a strong correlation
575 over similar timescales of weeks-years that was attributed to afterslip driving aftershock
576 production (Perfettini & Avouac, 2007; Barbot et al., 2009). Here we believe the lack of an
577 apparent correlation highlights the more prominent effect of viscoelastic relaxation occurring in a

578 back-arc extensional setting that could be masking surface strain resulting from afterslip, and is an
579 effect that should be modeled and removed first before it can be determined whether an afterslip-
580 aftershock correlation exists or not.

581

582 **5.3 Frictional Behavior of Early Afterslip**

583 To determine whether a rate-state or velocity-strengthening frictional regime governs the
584 frictional behavior of the fault surface, where the former predicts a transient phase of slip
585 acceleration following rupture, while the latter expects a continuous deceleration (Perfettini and
586 Avouac, 2007), we attempt to resolve the earliest phase of the afterslip evolution in the minute-to-
587 hours following rupture. From our early afterslip model that constrains the slip evolution at a
588 sampling rate every five minutes, we can detect no transient phase of nucleation and acceleration
589 within the first few days, and instead find an almost continuous deceleration of afterslip following
590 an almost log-time decay. In addition, we find no evidence of accelerated aftershocks rates (Figure
591 7c), which would otherwise suggest a phase of possible afterslip acceleration (assuming the
592 afterslip-aftershock relation is valid over such a timescale). We note that the deviation of afterslip
593 at ~14 hours after rupture is likely an artifact as it is similar to deviations seen later in the time
594 series, which would otherwise suggest the fault experiences back-slip that then recovers, which is
595 physically unlikely and not predicted by either the velocity strengthening or rate-state laws. In
596 addition, when estimating the power spectral density of the residuals (where the velocity
597 strengthening prediction is removed from the time series), we find a weak periodicity at ~12 hours
598 (Fig S6), that could indicate these deviations are related to possible hydrologic, thermoelastic or
599 volcanic deformation recorded at GPS stations. Furthermore, when isolating the large deviation at
600 ~14 hours using the ICA approach we find its spatial pattern is inconsistent with a tectonic or

601 afterslip process, and instead find GPS motions are largest around the volcano and orientated in a
602 north-west direction (see supplement S5 for more details).

603 Finding afterslip exhibits no clear transient phase of acceleration, we assume its evolution
604 can be described by a simple velocity strengthening law, allowing us to estimate the frictional
605 properties of the fault surface from eq. (4), (Gualandi et al., 2014; Marone et al., 1991). This
606 relation models the evolution of afterslip on a velocity strengthening patch as a spring-block slider
607 system, where the a - b parameter describes how the frictional resistance of the sliding block
608 changes in response to a velocity step imposed by the mainshock. From this model we find a - b
609 values ranging from 10^{-4} - 10^{-2} , with values highest at shallower depths and on the Futugawa fault
610 (Figure 8). Such small a - b values are indicative of a frictional surface that is slightly velocity-
611 strengthening, which under the appropriate loading conditions can undergo either creep or sustain
612 instabilities, termed a compliant field (Boatwright & Cocco, 1996). Such a compliant frictional
613 regime could explain why both aftershocks and afterslip are found to occur along both the
614 Futugawa and Hinagu faults, which is a behavior also found following the 2009 L'Aquila and 2015
615 Illapel earthquakes (Gualandi et al., 2014; Frank et al., 2017).

616

617

618 **6. Conclusions**

619

620 Using an independent component filtering technique to track the earliest evolution of aseismic
621 moment release, when rates are highest, reveals it amounts to $\sim 1\%$ of the coseismic moment within
622 the first hour ($M_w=5.7$), and $\sim 4\%$ ($M_w=6.1$) by the end of the first day (within the top 5 km of the
623 crust). This suggests we can be confident that the balanced slip-depth distribution (i.e., a lack of a

624 shallow slip deficit) found for the mainshock (that is constrained by geodetic data that spans the
625 mainshock and includes early postseismic slip), is largely reflective of the coseismic rupture
626 process, and has minimal contamination from rapid afterslip. Resolving the early kinematics of the
627 afterslip process also us to understand the frictional regime that governs the afterslip process.
628 Within the first few hours following rupture, afterslip exhibits no evidence of a delayed nucleation
629 and acceleration phase that is predicted by a full rate-and-state behavior, and instead afterslip
630 patches undergo immediate deceleration following rupture that is consistent with a simple
631 velocity-strengthening friction law indicating steady-state relaxation (i.e., no dependence on the
632 state-variable). Lastly, even within the first minutes-to-hours following the rupture there still
633 seems to be a close relation between afterslip and the cumulative number of aftershocks, a behavior
634 that is similar to that found following other earthquakes over longer timescales of months-years,
635 suggesting that afterslip could still influence aftershock production during these early periods.

636

637 **Acknowledgements**

638 **General:** We would like to thank Yuri Fialko and one anonymous reviewer for their helpful
639 suggestions. We also thank David Bekaert and Adriano Gualandi for helpful discussions.

640 **Funding:** Part of this research was supported by the NASA Earth Surface and Interior focus area
641 and performed at the Jet Propulsion Laboratory, California Institute of Technology. Funding for
642 this project was provided under a NASA Postdoctoral Program fellowship to C. Milliner
643 administered by the Universities Space and Research Association through a contract with NASA,
644 and a NASA ESI grant NNX16AL17G awarded to R. Bürgmann. **Author contributions:** C.M.
645 and R.B. developed the framework of the study. C.M. performed postprocessing of GPS data and
646 developed the inverse scheme. T.W. processed the Sentinel InSAR data, A.I. helped with

647 analysis of seismicity data and C.L. helped processing the ALOS-2 scenes. All authors
648 participated in manuscript revision. **Competing interests:** The authors declare that they have no
649 competing interests. **Data and materials availability:** GPS raw and filtered time series are
650 available as supplementary files and can be downloaded from the online open access data
651 repository site Zenodo (<https://doi.org/10.5281/zenodo.3522444>)

652

653

654

655 **References**

- 656 Argus, D.F., Gordon, R.G. (1991). No-net-rotation model of current plate velocities
657 incorporating plate motion model NUVEL-1. *Geophys. Res. Lett.* 18, 2039–2042.
658 <https://doi.org/10.1029/91GL01532>
- 659 Asano, K., Iwata, T. (2016). Source rupture processes of the foreshock and mainshock in the
660 2016 Kumamoto earthquake sequence estimated from the kinematic waveform inversion
661 of strong motion data. *Earth Planets Space* 68, 147. [https://doi.org/10.1186/s40623-016-](https://doi.org/10.1186/s40623-016-0519-9)
662 [0519-9](https://doi.org/10.1186/s40623-016-0519-9)
- 663 Barbot, S., Fialko, Y. and Sandwell, D., 2008. Effect of a compliant fault zone on the inferred
664 earthquake slip distribution. *Journal of Geophysical Research: Solid Earth*, 113(B6).
- 665 Barbot, S., Fialko, Y. (2010). A unified continuum representation of post-seismic relaxation
666 mechanisms: semi-analytic models of afterslip, poroelastic rebound and viscoelastic flow.
667 *Geophys. J. Int.* 182, 1124–1140. <https://doi.org/10.1111/j.1365-246X.2010.04678.x>
- 668 Biot, M.A. (1956). Theory of Propagation of Elastic Waves in a Fluid-Saturated Porous Solid. II.
669 Higher Frequency Range. *J. Acoust. Soc. Am.* 28, 179–191.
670 <https://doi.org/10.1121/1.1908241>
- 671 Boatwright, J. & Cocco, M., 1996. Frictional constraints on crustal faulting, *J. geophys. Res.*,
672 101(B6), 13 895–13 909
- 673 Brooks, B.A., Minson, S.E., Glennie, C.L., Nevitt, J.M., Dawson, T., Rubin, R., Ericksen, T.L.,
674 Lockner, D., Hudnut, K., Langenheim, V. and Lutz, A. (2017). Buried shallow fault slip
675 from the South Napa earthquake revealed by near-field geodesy. *Science advances*, 3(7),
676 p.e1700525. doi: 10.1126/sciadv.1700525
- 677 Byerlee, J., (1978). Friction of Rocks, in: Byerlee, J.D., Wyss, M. (Eds.), *Rock Friction and*
678 *Earthquake Prediction, Contributions to Current Research in Geophysics (CCRG)*.
679 Birkhäuser Basel, Basel, pp. 615–626. https://doi.org/10.1007/978-3-0348-7182-2_4
- 680 Chen, C.W., Zebker, H.A. (2001). Two-dimensional phase unwrapping with use of statistical
681 models for cost functions in nonlinear optimization. *JOSA A* 18, 338–351.
682 <https://doi.org/10.1364/JOSAA.18.000338>

- 683 Cohen-Waeber, J., Bürgmann, R., Chaussard, E., Giannico, C. and Ferretti, A. (2018).
684 Spatiotemporal Patterns of Precipitation-Modulated Landslide Deformation From
685 Independent Component Analysis of InSAR Time Series. *Geophysical Research*
686 *Letters*, 45(4), pp.1878-1887. <https://doi.org/10.1002/2017GL075950>
- 687 Dieterich, J. (1994). A constitutive law for rate of earthquake production and its application to
688 earthquake clustering. *J. Geophys. Res. Solid Earth* 99, 2601–2618.
689 <https://doi.org/10.1029/93JB02581>
- 690 Dieterich, J. (2007), Applications of rate- and state-dependent friction to models of fault slip and
691 earthquake occurrence, *Treatise on Geophysics*, 4, 107-129.
- 692 Dolan, J.F. and Haravitch, B.D. (2014). How well do surface slip measurements track slip at
693 depth in large strike-slip earthquakes? The importance of fault structural maturity in
694 controlling on-fault slip versus off-fault surface deformation. *Earth and Planetary*
695 *Science Letters*, 388, pp.38-47.
- 696 Dong, D., Fang, P., Bock, Y., Webb, F., Prawirodirdjo, L., Kedar, S., Jamason, P. (2006).
697 Spatiotemporal filtering using principal component analysis and Karhunen-Loeve
698 expansion approaches for regional GPS network analysis. *J. Geophys. Res. Solid Earth*
699 111, B03405. <https://doi.org/10.1029/2005JB003806>
- 700 Du, Y., Aydin, A., Segall, P. (1992). Comparison of various inversion techniques as applied to
701 the determination of a geophysical deformation model for the 1983 Borah Peak
702 earthquake. *Bull. Seismol. Soc. Am.* 82, 1840–1866.
- 703 Fattahi, H., Amelung, F., Chaussard, E., Wdowinski, S. (2015). Coseismic and postseismic
704 deformation due to the 2007 M5.5 Ghazaband fault earthquake, Balochistan, Pakistan.
705 *Geophys. Res. Lett.* 42, 3305–3312. <https://doi.org/10.1002/2015GL063686>
- 706 Fialko, Y., Simons, M., & Agnew, D. (2001). The complete (3-D) surface displacement field in
707 the epicentral area of the 1999 Mw7. 1 Hector Mine earthquake, California, from space
708 geodetic observations. *Geophysical research letters*, 28(16), 3063-3066.
709 <https://doi.org/10.1029/2001GL013174>
- 710 Fialko, Y., Sandwell, D., Simons, M., Rosen, P. (2005). Three-dimensional deformation caused
711 by the Bam, Iran, earthquake and the origin of shallow slip deficit. *Nature* 435, 295.
712 <https://doi.org/10.1038/nature03425>
- 713 Fielding, E.J., Lundgren, P.R., Bürgmann, R. and Funning, G.J. (2009). Shallow fault-zone
714 dilatancy recovery after the 2003 Bam earthquake in Iran. *Nature*, 458(7234), p.64. doi:
715 <https://doi.org/10.1038/nature07817>
- 716 Frank, W.B., Poli, P., Perfettini, H. (2017). Mapping the rheology of the Central Chile
717 subduction zone with aftershocks. *Geophys. Res. Lett.* 44, 5374–5382.
718 <https://doi.org/10.1002/2016GL072288>
- 719 Freed, A.M. (2007). Afterslip (and only afterslip) following the 2004 Parkfield, California,
720 earthquake. *Geophys. Res. Lett.* 34(6). <https://doi.org/10.1029/2006GL029155>
- 721 Freed, A.M., Bürgmann, R., Calais, E., Freymueller, J., Hreinsdóttir, S. (2006). Implications of
722 deformation following the 2002 Denali, Alaska, earthquake for postseismic relaxation
723 processes and lithospheric rheology. *J. Geophys. Res.* 111(B1).
724 <https://doi.org/10.1029/2005JB003894>
- 725 Fujiwara, S., Yarai, H., Kobayashi, T., Morishita, Y., Nakano, T., Miyahara, B., Nakai, H.,
726 Miura, Y., Ueshiba, H., Kakiage, Y., Une, H. (2016). Small-displacement linear surface
727 ruptures of the 2016 Kumamoto earthquake sequence detected by ALOS-2 SAR

728 interferometry. *Earth Planets Space* 68(1), 160. [https://doi.org/10.1186/s40623-016-0534-](https://doi.org/10.1186/s40623-016-0534-x)
729 x

730 Fukuda, J., Johnson, K.M., Larson, K.M., Miyazaki, S. (2009). Fault friction parameters inferred
731 from the early stages of afterslip following the 2003 Tokachi-oki earthquake. *J. Geophys.*
732 *Res.* 114(B4). <https://doi.org/10.1029/2008JB006166>

733 Gold, R.D., Reitman, N.G., Briggs, R.W., Barnhart, W.D., Hayes, G.P., Wilson, E. (2015). On-
734 and off-fault deformation associated with the September 2013 Mw 7.7 Balochistan
735 earthquake: Implications for geologic slip rate measurements. *Tectonophysics* 660, 65–
736 78. <https://doi.org/10.1016/j.tecto.2015.08.019>

737 Gomberg, J., Johnson, P. (2005). Dynamic triggering of earthquakes. *Nature* 437, 830.
738 <https://doi.org/10.1038/437830a>

739 Gualandi, A., Serpelloni, E., Belardinelli, M.E. (2014). Space–time evolution of crustal
740 deformation related to the Mw 6.3, 2009 L’Aquila earthquake (central Italy) from
741 principal component analysis inversion of GPS position time-series. *Geophys. J. Int.* 197,
742 174–191. <https://doi.org/10.1093/gji/ggt522>

743 Harnessing the GPS Data Explosion for Interdisciplinary Science [WWW Document], *Eos*. URL
744 [https://eos.org/project-updates/harnessing-the-gps-data-explosion-for-interdisciplinary-](https://eos.org/project-updates/harnessing-the-gps-data-explosion-for-interdisciplinary-science)
745 [science](https://eos.org/project-updates/harnessing-the-gps-data-explosion-for-interdisciplinary-science) (accessed 5.14.2019).

746 Hao, J., C. Ji, and Z. Yao (2016), Slip history of the 2016 Mw 7.0 Kumamoto earthquake:
747 Intraplate rupture in complex tectonic environment, *Geophys. Res. Lett.*, 43,
748 doi:10.1002/2016GL071543.

749 Helmstetter, A., Shaw, B.E. (2009). Afterslip and aftershocks in the rate-and-state friction law. *J.*
750 *Geophys. Res. Solid Earth* 114(B1). <https://doi.org/10.1029/2007JB005077>

751 Hill, E.M., Borrero, J.C., Huang, Z., Qiu, Q., Banerjee, P., Natawidjaja, D.H., Elosegui, P., Fritz,
752 H.M., Suwargadi, B.W., Pranantyo, I.R. and Li, L. (2012). The 2010 Mw 7.8 Mentawai
753 earthquake: Very shallow source of a rare tsunami earthquake determined from tsunami
754 field survey and near-field GPS data. *Journal of Geophysical Research: Solid*
755 *Earth*, 117(B6). <https://doi.org/10.1029/2012JB009159>

756 Hreinsdóttir, S., Freymueller, J.T., Bürgmann, R. and Mitchell, J. (2006). Coseismic deformation
757 of the 2002 Denali fault earthquake: Insights from GPS measurements. *Journal of*
758 *Geophysical Research: Solid Earth*, 111(B3). doi: 10.1029/2005JB003676

759 Huang, M.H., Fielding, E.J., Dickinson, H., Sun, J., Gonzalez-Ortega, J.A., Freed, A.M. and
760 Bürgmann, R. (2017). Fault geometry inversion and slip distribution of the 2010 Mw 7.2
761 El Mayor-Cucapah earthquake from geodetic data. *Journal of Geophysical Research:*
762 *Solid Earth*, 122(1), pp.607-621. <https://doi.org/10.1002/2016JB012858>

763 Hyvärinen, A., Oja, E. (2000). Independent component analysis: algorithms and applications.
764 *Neural Netw.* 13, 411–430. [https://doi.org/10.1016/S0893-6080\(00\)00026-5](https://doi.org/10.1016/S0893-6080(00)00026-5)

765 Ikeda, M., Toda, S., Kobayashi, S., Ohno, Y., Nishizaka, N., & Ohno, I. (2009). Tectonic model
766 and fault segmentation of the Median Tectonic Line active fault system on Shikoku,
767 Japan. *Tectonics*, 28(5). <https://doi.org/10.1029/2008TC002349>

768 Jiang, H., Feng, G., Wang, T., Bürgmann, R. (2017). Toward full exploitation of coherent and
769 incoherent information in Sentinel-1 TOPS data for retrieving surface displacement:
770 Application to the 2016 Kumamoto (Japan) earthquake. *Geophysical Research*
771 *Letters*, 44(4), 1758-1767. <https://doi.org/10.1002/2016GL072253>

- 772 Kaneko, Y., Fialko, Y. (2011). Shallow slip deficit due to large strike-slip earthquakes in
773 dynamic rupture simulations with elasto-plastic off-fault response. *Geophys. J. Int.* 186,
774 1389–1403. <https://doi.org/10.1111/j.1365-246X.2011.05117>.
- 775 Kato, A., Fukuda, J., Nakagawa, S., Obara, K. (2016). Foreshock migration preceding the 2016
776 Mw 7.0 Kumamoto earthquake, Japan. *Geophys. Res. Lett.* 43, 8945–8953.
777 <https://doi.org/10.1002/2016GL070079>
- 778 Kobayashi, H., Koketsu, K., Miyake, H. (2017). Rupture processes of the 2016 Kumamoto
779 earthquake sequence: Causes for extreme ground motions. *Geophys. Res. Lett.* 44, 6002–
780 6010. <https://doi.org/10.1002/2017GL073857>
- 781 Kositsky, A.P., Avouac, J.-P. (2010). Inverting geodetic time series with a principal component
782 analysis-based inversion method. *J. Geophys. Res. Solid Earth* 115(B3).
783 <https://doi.org/10.1029/2009JB006535>
- 784 Lange, D., Bedford, J.R., Moreno, M., Tilmann, F., Baez, J.C., Bevis, M., Krüger, F. (2014).
785 Comparison of postseismic afterslip models with aftershock seismicity for three
786 subduction-zone earthquakes: Nias 2005, Maule 2010 and Tohoku 2011. *Geophys. J. Int.*
787 199, 784–799. <https://doi.org/10.1093/gji/ggu292>
- 788 Le, Q.V., Karpenko, A., Ngiam, J., Ng, A.Y. (2011). ICA with Reconstruction Cost for Efficient
789 Overcomplete Feature Learning, in: Shawe-Taylor, J., Zemel, R.S., Bartlett, P.L., Pereira,
790 F., Weinberger, K.Q. (Eds.), *Advances in Neural Information Processing Systems* 24.
791 Curran Associates, Inc., pp. 1017–1025.
- 792 Leprince, S., Ayoub, F., Klinger, Y., Avouac, J. (2007). Co-Registration of Optically Sensed
793 Images and Correlation (COSI-Corr): an operational methodology for ground
794 deformation measurements, in: 2007 IEEE International Geoscience and Remote Sensing
795 Symposium. Presented at the 2007 IEEE International Geoscience and Remote Sensing
796 Symposium, pp. 1943–1946. <https://doi.org/10.1109/IGARSS.2007.4423207>
- 797 Liang, C. and Fielding, E.J. (2017). Interferometry with ALOS-2 full-aperture ScanSAR
798 data. *IEEE Transactions on Geoscience and Remote Sensing*, 55(5), pp.2739-2750.
799 [10.1109/TGRS.2017.2653190](https://doi.org/10.1109/TGRS.2017.2653190)
- 800 Lienkaemper, J.J., DeLong, S.B., Domrose, C.J., Rosa, C.M. (2016). Afterslip Behavior
801 following the 2014 M 6.0 South Napa Earthquake with Implications for Afterslip
802 Forecasting on Other Seismogenic Faults. *Seismol. Res. Lett.* 87, 609–619.
803 <https://doi.org/10.1785/0220150262>
- 804 Lin, A., Chen, P., Satsukawa, T., Sado, K., Takahashi, N., Hirata, S. (2017). Millennium
805 Recurrence Interval of Morphogenic Earthquakes on the Seismogenic Fault Zone That
806 Triggered the 2016 Mw 7.1 Kumamoto Earthquake, Southwest Japan Millennium
807 Recurrence Interval of Morphogenic Earthquakes. *Bull. Seismol. Soc. Am.* 107, 2687–
808 2702. <https://doi.org/10.1785/0120170149>
- 809 Lindsey, E.O., Sahakian, V.J., Fialko, Y., Bock, Y., Barbot, S. and Rockwell, T.K., 2014.
810 Interseismic strain localization in the San Jacinto fault zone. *Pure and Applied*
811 *Geophysics*, 171(11), pp.2937-2954.
- 812 Liu, B., Dai, W., Liu, N. (2017). Extracting seasonal deformations of the Nepal Himalaya region
813 from vertical GPS position time series using Independent Component Analysis. *Adv.*
814 *Space Res.*, *BDS/GNSS+: Recent Progress and New Applications - Part 2* 60, 2910–
815 2917. <https://doi.org/10.1016/j.asr.2017.02.028>
- 816 Liu, X. and Xu, W. (2019). Logarithmic Model Joint Inversion Method for Coseismic and
817 Postseismic Slip: Application to the 2017 Mw 7.3 Sarpol Zahāb Earthquake,

818 Iran. *Journal of Geophysical Research: Solid Earth*, 124(11), pp.12034-12052.
819 doi.org/10.1029/2019JB017953

820 Lorenzetti E, Tullis TE. (1989). Geodetic predictions of a strike-slip fault model: implications for
821 intermediate-and short-term earthquake prediction. *J. Geophys. Res.* 94:12343–
822 6. <https://doi.org/10.1029/JB094iB09p12343>

823 Ma, S. (2008). A physical model for widespread near-surface and fault zone damage induced by
824 earthquakes: *Geochem. Geophys. Geosystems* 9(11).
825 <https://doi.org/10.1029/2008GC002231>

826 Marone, C.J., Scholtz, C.H., Bilham, R. (1991). On the mechanics of earthquake afterslip. *J.*
827 *Geophys. Res. Solid Earth* 96, 8441–8452. <https://doi.org/10.1029/91JB00275>

828 Marone, C. (1998). Laboratory-Derived Friction Laws and Their Application to Seismic
829 Faulting. *Annu. Rev. Earth Planet. Sci.* 26, 643–696.
830 <https://doi.org/10.1146/annurev.earth.26.1.643>

831 Milliner, C.W.D., Dolan, J.F., Hollingsworth, J., Leprince, S., Ayoub, F., Sammis, C.G. (2015).
832 Quantifying near-field and off-fault deformation patterns of the 1992 Mw 7.3 Landers
833 earthquake. *Geochem. Geophys. Geosystems* 16, 1577–1598.
834 <https://doi.org/10.1002/2014GC005693>

835 Miyazaki, Larson, K.M. (2008). Coseismic and early postseismic slip for the 2003 Tokachi-oki
836 earthquake sequence inferred from GPS data. *Geophys. Res. Lett.* 35 (4). [https://doi.org](https://doi.org/10.1029/2007GL032309)
837 [/10.1029/2007GL032309](https://doi.org/10.1029/2007GL032309).

838 Miyakawa, A., Sumita, T., Okubo, Y., Okuwaki, R., Otsubo, M., Uesawa, S., Yagi, Y. (2016).
839 Volcanic magma reservoir imaged as a low-density body beneath Aso volcano that
840 terminated the 2016 Kumamoto earthquake rupture. *Earth Planets Space* 68, 208.
841 <https://doi.org/10.1186/s40623-016-0582-2>

842 Moore, J.D.P., Yu, H., Tang, C.-H., Wang, T., Barbot, S., Peng, D., Masuti, S., Dauwels, J., Hsu,
843 Y.-J., Lambert, V., Nanjundiah, P., Wei, S., Lindsey, E., Feng, L., Shibazaki, B. (2017).
844 Imaging the distribution of transient viscosity after the 2016 Mw 7.1 Kumamoto
845 earthquake. *Science* 356, 163–167. <https://doi.org/10.1126/science.aal3422>

846 Nimiya, H., Ikeda, T., Tsuji, T. (2017). Spatial and temporal seismic velocity changes on Kyushu
847 Island during the 2016 Kumamoto earthquake. *Sci. Adv.* 3, e1700813.
848 <https://doi.org/10.1126/sciadv.1700813>

849 North, G.R., Bell, T.L., Cahalan, R.F., Moeng, F.J. (1982). Sampling Errors in the Estimation of
850 Empirical Orthogonal Functions. *Mon. Weather Rev.* 110, 699–706.
851 <https://doi.org/10.1175/1520-0493>

852 Okada, Y. (1992). Internal deformation due to shear and tensile faults in a half-space. *Bull.*
853 *Seismol. Soc. Am.* 82, 1018–1040.

854 Ozawa, T., Fujita, E., Ueda, H. (2016). Crustal deformation associated with the 2016 Kumamoto
855 Earthquake and its effect on the magma system of Aso volcano. *Earth Planets Space*
856 68(1), 186. <https://doi.org/10.1186/s40623-016-0563-5>

857 Perfettini, H., Avouac, J.-P. (2007). Modeling afterslip and aftershocks following the 1992
858 Landers earthquake. *J. Geophys. Res. Solid Earth* 112(B7).

859 Perfettini, H., and J.-P. Ampuero (2008), Dynamics of a velocity strengthening fault region:
860 Implications for slow earthquakes and postseismic slip, *J. Geophys. Res.*, 113, B09411,
861 [doi:10.1029/2007JB005398](https://doi.org/10.1029/2007JB005398). doi.org/10.1029/2006JB004399

862 Petit, G., Luzum, B., 2010. IERS Conventions (2010) (No. IERS-TN-36). Bureau International
863 Des Poids Et Mesures Sevres (France).

- 864 Pitarka, A., Dalguer, L.A., Day, S.M., Somerville, P.G., Dan, K. (2009). Numerical Study of
865 Ground-Motion Differences between Buried-Rupturing and Surface-Rupturing
866 Earthquakes Numerical Study of Ground-Motion Differences between Buried-Rupturing
867 and Surface-Rupturing Earthquakes. *Bull. Seismol. Soc. Am.* 99, 1521–1537.
868 <https://doi.org/10.1785/0120080193>
- 869 Platt, J.P., Leggett, J.K. and Alam, S., 1988. Slip vectors and fault mechanics in the Makran
870 accretionary wedge, southwest Pakistan. *Journal of Geophysical Research: Solid
871 Earth*, 93(B7), pp.7955-7973.
- 872 Pollitz, F.F. (2001). Mantle Flow Beneath a Continental Strike-Slip Fault: Postseismic
873 Deformation After the 1999 Hector Mine Earthquake. *Science* 293, 1814–1818.
874 <https://doi.org/10.1126/science.1061361>
- 875 Pollitz, F.F., Kobayashi, T., Yurai, H., Shibasaki, B., Matsumoto, T. (2017). Viscoelastic lower
876 crust and mantle relaxation following the 14–16 April 2016 Kumamoto, Japan,
877 earthquake sequence. *Geophys. Res. Lett.* 44, 8795–8803.
878 <https://doi.org/10.1002/2017GL074783>
- 879 Ragon, T., Sladen, A., Bletery, Q., Vergnolle, M., Cavalié, O., Avallone, A., Balestra, J. and
880 Delouis, B. (2019). Joint Inversion of Coseismic and Early Postseismic Slip to Optimize
881 the Information Content in Geodetic Data: Application to the 2009 M w 6.3 L'Aquila
882 Earthquake, Central Italy. *Journal of Geophysical Research: Solid Earth*, 124(10),
883 pp.10522-10543.
- 884 Rockwell, T.K., Lindvall, S., Dawson, T., Langridge, R., Lettis, W., Klinger, Y. (2002). Lateral
885 Offsets on Surveyed Cultural Features Resulting from the 1999 İzmit and Düzce
886 Earthquakes, Turkey. *Bull. Seismol. Soc. Am.* 92, 79–94.
887 <https://doi.org/10.1785/0120000809>
- 888 Ross, Z.E., White, M.C., Vernon, F.L., Ben-Zion, Y. (2016). An Improved Algorithm for Real-
889 Time S-Wave Picking with Application to the (Augmented) ANZA Network in Southern
890 California Improved Algorithm for Real-Time S-Wave Picking with Application to
891 ANZA. *Bull. Seismol. Soc. Am.* 106, 2013–2022. <https://doi.org/10.1785/0120150230>
- 892 Rousset, B., Barbot, S., Avouac, J.-P., Hsu, Y.-J. (2012). Postseismic deformation following the
893 1999 Chi-Chi earthquake, Taiwan: Implication for lower-crust rheology *J. Geophys. Res.*
894 *Solid Earth* 117(B12). <https://doi.org/10.1029/2012JB009571>
- 895 Sagiya, T., S. Miyazaki, and T. Tada (2000), Continuous GPS array and present-day crustal
896 deformation of Japan, *Pure Appl. Geophys.*, 157, 2303–2322.
- 897 Scholz CH. (1988). The critical slip distance for seismic faulting. *Nature* 336:761–63.
898 <https://doi.org/10.1038/336761a0>
- 899 Scott, C., Champenois, J., Klinger, Y., Nissen, E., Maruyama, T., Chiba, T., Arrowsmith, R.,
900 (2016) 2016 M7 Kumamoto, Japan, Earthquake Slip Field Derived From a Joint
901 Inversion of Differential Lidar Topography, Optical Correlation, and InSAR Surface
902 Displacements. *Geophys. Res. Lett.* 46(12), 6341-6351.
903 <https://doi.org/10.1029/2019GL082202>
- 904 Scott, C.P., Arrowsmith, J.R., Nissen, E., Lajoie, L., Maruyama, T., Chiba, T. (2018). The M7
905 2016 Kumamoto, Japan, Earthquake: 3-D Deformation Along the Fault and Within the
906 Damage Zone Constrained From Differential Lidar Topography. *J. Geophys. Res. Solid
907 Earth* 123, 6138–6155. <https://doi.org/10.1029/2018JB015581>
- 908 Serpelloni, E., Faccenna, C., Spada, G., Dong, D., Williams, S.D.P. (2013). Vertical GPS ground
909 motion rates in the Euro-Mediterranean region: New evidence of velocity gradients at

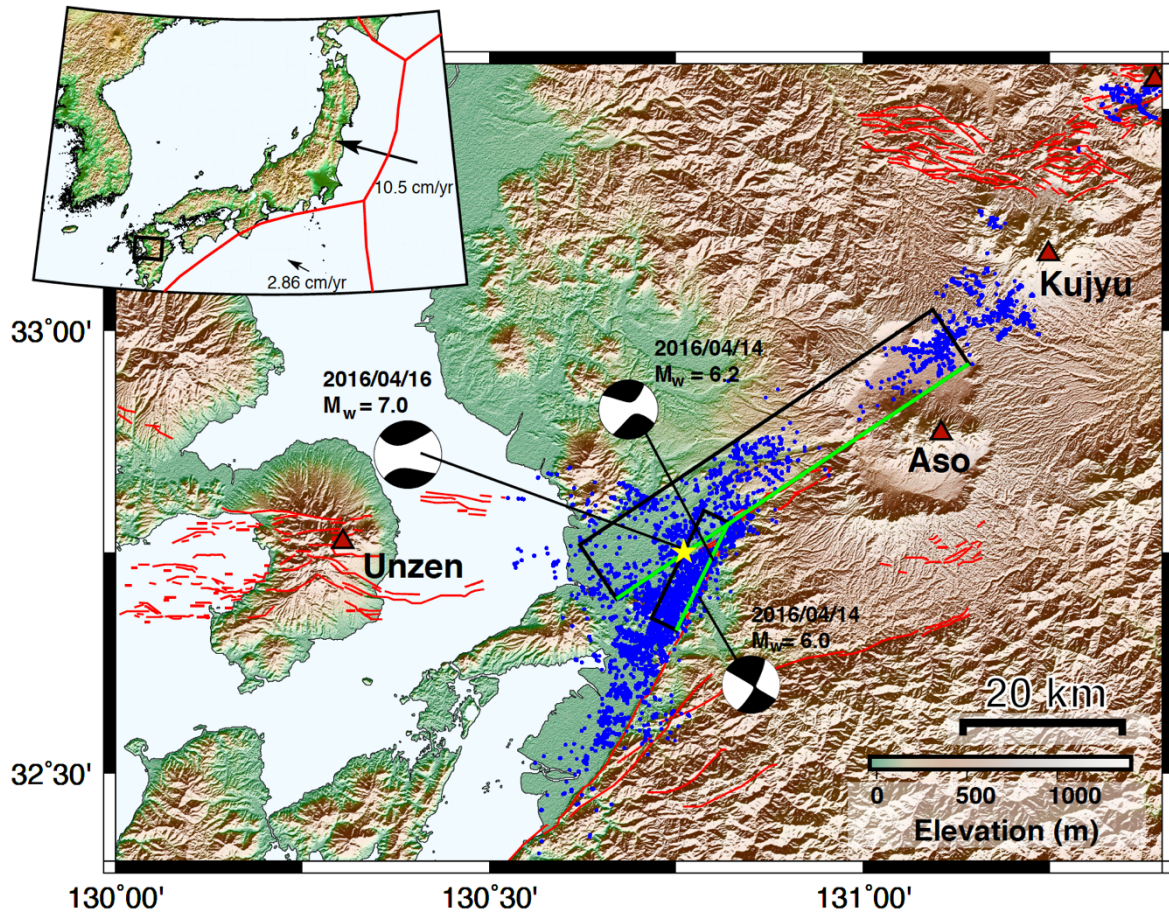
910 different spatial scales along the Nubia-Eurasia plate boundary. *J. Geophys. Res. Solid*
 911 *Earth* 118, 6003–6024. <https://doi.org/10.1002/2013JB010102>
 912 Shelly, D.R., Hardebeck, J.L., Ellsworth, W.L., Hill, D.P. (2016). A new strategy for earthquake
 913 focal mechanisms using waveform-correlation-derived relative polarities and cluster
 914 analysis: Application to the 2014 Long Valley Caldera earthquake swarm. *J. Geophys.*
 915 *Res. Solid Earth* 121, 8622–8641. <https://doi.org/10.1002/2016JB013437>
 916 Shirahama, Y., Yoshimi, M., Awata, Y., Maruyama, T., Azuma, T., Miyashita, Y., Mori, H.,
 917 Imanishi, K., Takeda, N., Ochi, T., Otsubo, M., Asahina, D., Miyakawa, A. (2016).
 918 Characteristics of the surface ruptures associated with the 2016 Kumamoto earthquake
 919 sequence, central Kyushu, Japan. *Earth Planets Space* 68, 191.
 920 <https://doi.org/10.1186/s40623-016-0559-1>
 921 Somerville, P.G. (2003). Magnitude scaling of the near fault rupture directivity pulse. *Phys.*
 922 *Earth Planet. Inter.*, The quantitative prediction of strong-motion and the physics of
 923 earthquake sources 137, 201–212. [https://doi.org/10.1016/S0031-9201\(03\)00015-3](https://doi.org/10.1016/S0031-9201(03)00015-3)
 924 Stuart, W.D. (1988) Forecast model for great earthquakes at the Nankai Trough subduction
 925 zone. *PAGEOPH* 126, 619–641. <https://doi.org/10.1007/BF00879012>
 926 Tajima, Y., Hasenaka, T., Torii, M. (2017). Effects of the 2016 Kumamoto earthquakes on the
 927 Aso volcanic edifice. *Earth Planets Space* 69, 63. [https://doi.org/10.1186/s40623-017-](https://doi.org/10.1186/s40623-017-0646-y)
 928 [0646-y](https://doi.org/10.1186/s40623-017-0646-y)
 929 Toda, S., Stein, R.S., Beroza, G.C. and Marsan, D. (2012). Aftershocks halted by static stress
 930 shadows. *Nature Geoscience*, 5(6), p.410. doi.org/10.1038/ngeo1465
 931 Toda, S., Kaneda, H., Okada, S., Ishimura, D., Mildon, Z.K. (2016). Slip-partitioned surface
 932 ruptures for the Mw 7.0 16 April 2016 Kumamoto, Japan, earthquake. *Earth Planets*
 933 *Space* 68. <https://doi.org/10.1186/s40623-016-0560-8>
 934 Tse, S.T., and Rice., J.R. (1986) Crustal earthquake in stability in relation to the depth variation
 935 of frictional slip properties, *J. Geophys. Res.*, 91, 9452-9472.
 936 <https://doi.org/10.1029/JB091iB09p09452>
 937 Tsuji, T., Ishibashi, J., Ishitsuka, K., Kamata, R. (2017). Horizontal sliding of kilometre-scale hot
 938 spring area during the 2016 Kumamoto earthquake. *Sci. Rep.* 7.
 939 <https://doi.org/10.1038/srep42947>
 940 Twardzik, C., Vergnolle, M., Sladen, A. and Avallone, A. (2019). Unravelling the contribution
 941 of early postseismic deformation using sub-daily GNSS positioning. *Scientific*
 942 *reports*, 9(1), pp.1-12. [/doi.org/10.1038/s41598-019-39038-z](https://doi.org/10.1038/s41598-019-39038-z)
 943 Utsu, T., Ogata, Y., S, R., Matsu'ura (1995). The Centenary of the Omori Formula for a Decay
 944 Law of Aftershock Activity. *J. Phys. Earth* 43, 1–33. <https://doi.org/10.4294/jpe1952.43.1>
 945 Wdowinski, S., Bock, Y., Zhang, J., Fang, P., Genrich, J. (1997). Southern California permanent
 946 GPS geodetic array: Spatial filtering of daily positions for estimating coseismic and
 947 postseismic displacements induced by the 1992 Landers earthquake. *J. Geophys. Res.*
 948 *Solid Earth* 102, 18057–18070. <https://doi.org/10.1029/97JB01378>
 949 Williams Simon D. P., Bock Yehuda, Fang Peng, Jamason Paul, Nikolaidis Rosanne M.,
 950 Prawirodirdjo Linette, Miller Meghan, Johnson Daniel J. (2004). Error analysis of
 951 continuous GPS position time series. *J. Geophys. Res. Solid Earth* 109.
 952 <https://doi.org/10.1029/2003JB002741>
 953 Xu, X., Tong, X., Sandwell, D.T., Milliner, C.W.D., Dolan, J.F., Hollingsworth, J., Leprince, S.,
 954 Ayoub, F. (2016). Refining the shallow slip deficit. *Geophys. J. Int.* 204, 1867–1886.
 955 <https://doi.org/10.1093/gji/ggv563>

956 Yagi, Y., Okuwaki, R., Enescu, B., Kasahara, A., Miyakawa, A., Otsubo, M. (2016). Rupture
957 process of the 2016 Kumamoto earthquake in relation to the thermal structure around Aso
958 volcano. *Earth Planets Space* 68, 118. <https://doi.org/10.1186/s40623-016-0492-3>
959 Yue, H., Ross, Z.E., Liang, C., Michel, S., Fattahi, H., Fielding, E., Moore, A., Liu, Z., Jia, B.
960 (2017). The 2016 Kumamoto Mw = 7.0 Earthquake: A Significant Event in a Fault-
961 Volcano System. *J. Geophys. Res. Solid Earth* 122, 9166–9183.
962 <https://doi.org/10.1002/2017JB014525>
963

964

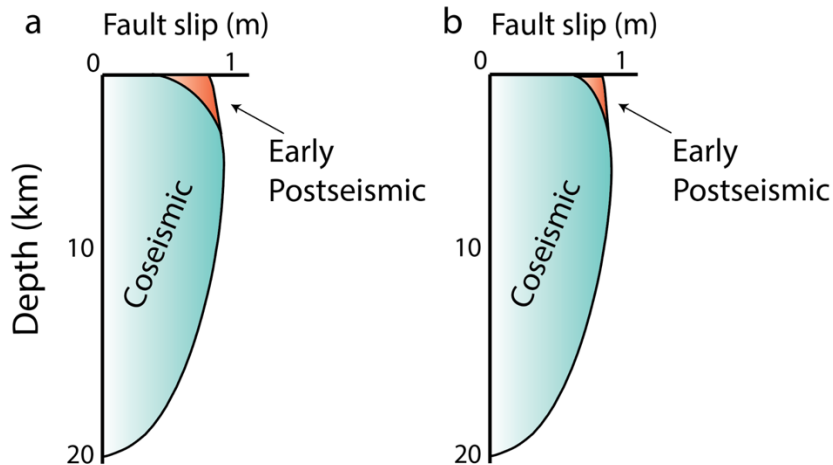
965 **Figures**

966



967

968 **Figure 1.** Location of the 2016 $M_w = 7.1$ Kumamoto earthquake and aftershocks on Kyushu
969 island. GCMT solutions of the mainshock and two foreshocks are filled in black, red lines show
970 surface traces of mapped geologic faults, blue dots show aftershocks from Yue et al. (2017), and
971 red triangles show location of active volcanoes. The black rectangles show the fault model used
972 in the coseismic inversion and green line the surface trace. Inset map shows the regional location
973 in south Japan, with plate boundaries shown as red lines and plate motion as vectors relative to
974 stable Eurasia in ITRF2014 (Argus and Gordon, 1991).



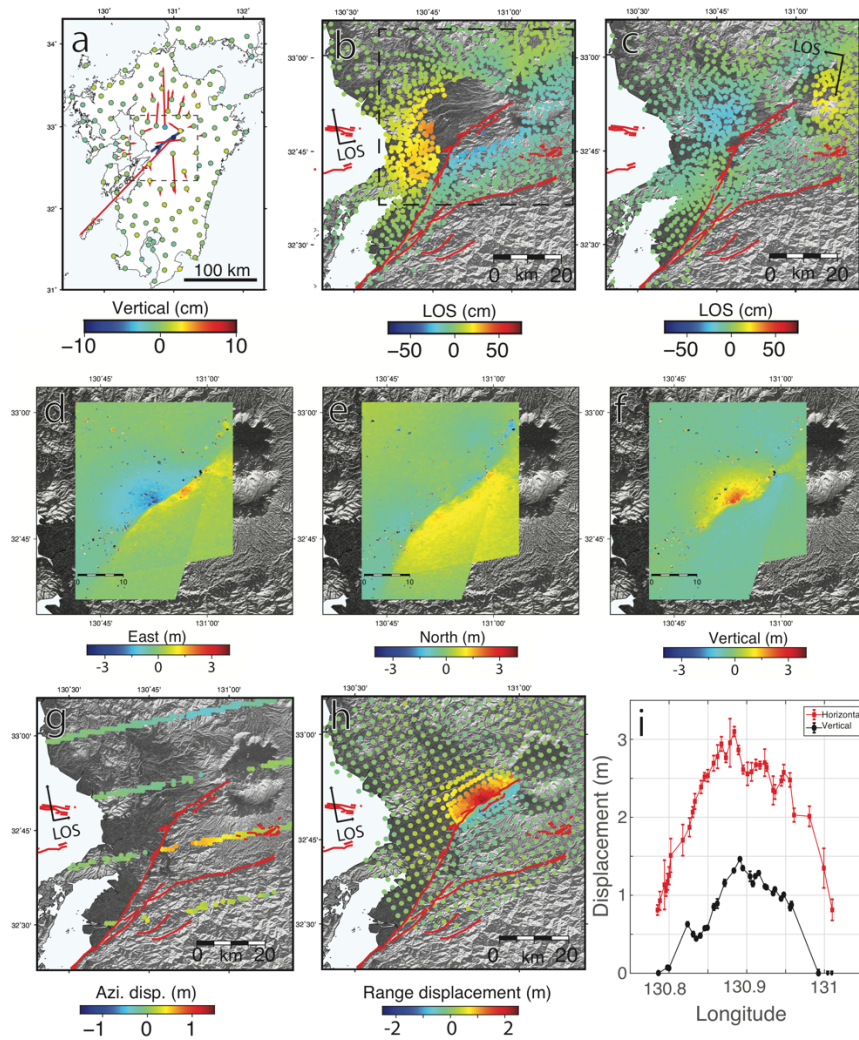
975

976 **Figure 2.** Simplified schematic illustrating end-member models of how early afterslip in the
 977 shallow crust may affect our understanding of coseismic slip deficits in the shallow crust (< 5 km
 978 depths). a) left shows the scenario where large coseismic slip deficits drive large and rapid
 979 afterslip, while b), right shows scenario where stored elastic strain in the shallow crust is mostly
 980 relieved coseismically with subdued coseismic slip deficits and a smaller contribution of strain
 981 release from afterslip. Distinguishing between these two endmember models requires constraining
 982 the rate of moment release as a function of depth within the first hours following rupture when
 983 afterslip rates are highest, with each model suggesting different behaviors as to how efficiently the
 984 dynamic rupture can propagate through the near-surface.

985

986

987

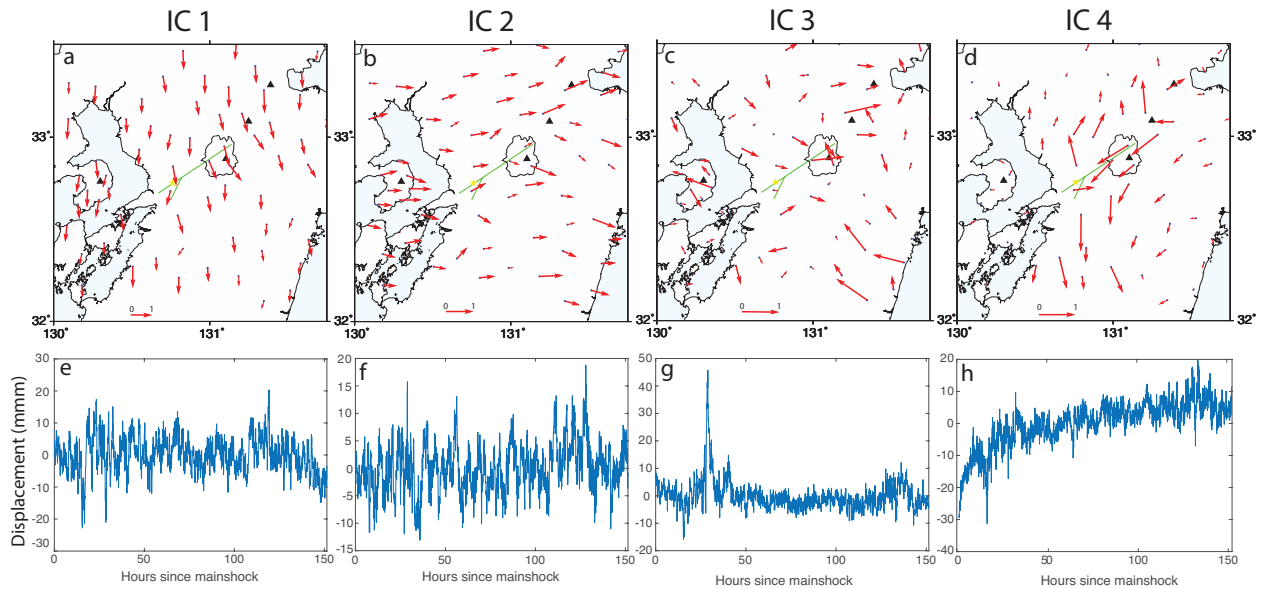


988

989 **Figure 3. Geodetic data used for the coseismic slip inversion.** a) and b) show ascending and
 990 descending Sentinel-1A InSAR, respectively, positive LOS is range increase c) shows horizontal
 991 (vectors) and vertical (colored dots) displacements from GPS. d-f) shows the 3D surface
 992 deformation resolved by decomposing multiple offsets maps from ALOS-2 satellite. g) and h)
 993 show azimuthal and range offset maps from Sentinel-1A imagery and i) shows the surface fault
 994 displacements, with the horizontal displacement (red line) derived from d) and e), and vertical
 995 (black line) from f).

996

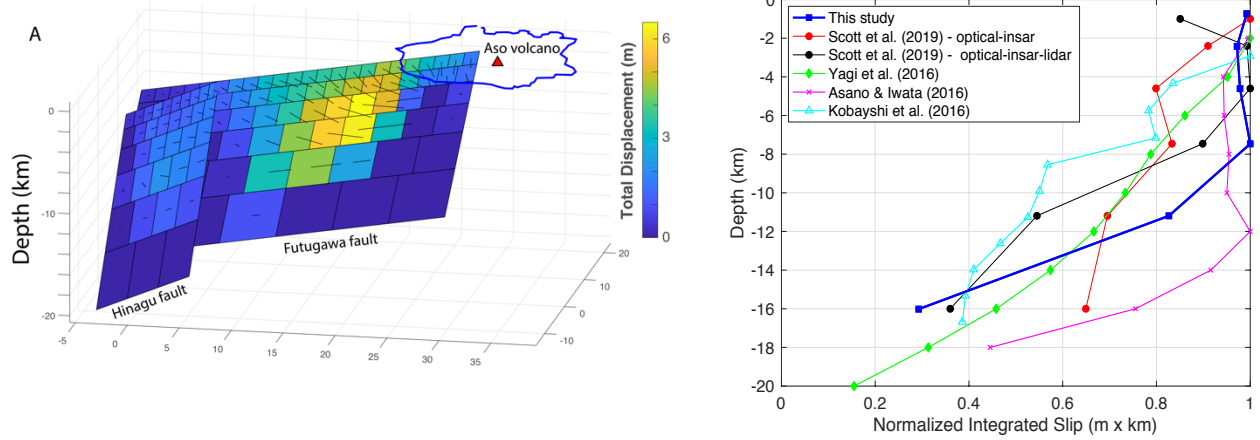
997



998

999

1000 **Figure 4.** Independent component analysis of the five-minute sampled horizontal GPS time series
 1001 during the early postseismic phase (first six days following rupture). Top row shows the spatial
 1002 responses (normalized to unit scale), and bottom the temporal components. Independent
 1003 components (columns) are ordered from left to right according to the amount of variance (see
 1004 section S1 and eq. S1 for method). The fourth component isolates the postseismic deformation
 1005 (green lines in top row show trace of Kumamoto rupture), while the first and second components
 1006 represent common-mode error of the north and east motions, respectively. The third component is
 1007 likely related to volcanic deformation due to the strong spatial responses (active volcanoes are
 1008 shown as black triangles and Aso caldera rim is outlined with black thin line).
 1009



1010

1011

1012

Figure 5. Oblique view towards NNW of coseismic slip model. a) The model is

1013 constrained by geodetic data shown in Figure 3 and illustrates slip variation with depth. Largest

1014 slip is located on the Futugawa fault adjacent to the Aso volcano (red triangle, with caldera rim

1015 outlined in blue). b) Slip-depth distribution from a) and comparison to other slip models. The range

1016 of behaviors illustrates the epistemic uncertainty due to use of different data and modeling

1017 approaches. Most models indicate near-surface slip is similar to that at depth, suggesting a low or

1018 almost no slip-deficit, as found in our result (thick blue line). The slip-depth curve is estimated by

1019 integrating slip at each depth interval and then normalizing by the largest value following Fialko

1020 et al. (2005).

1021

1022

1023

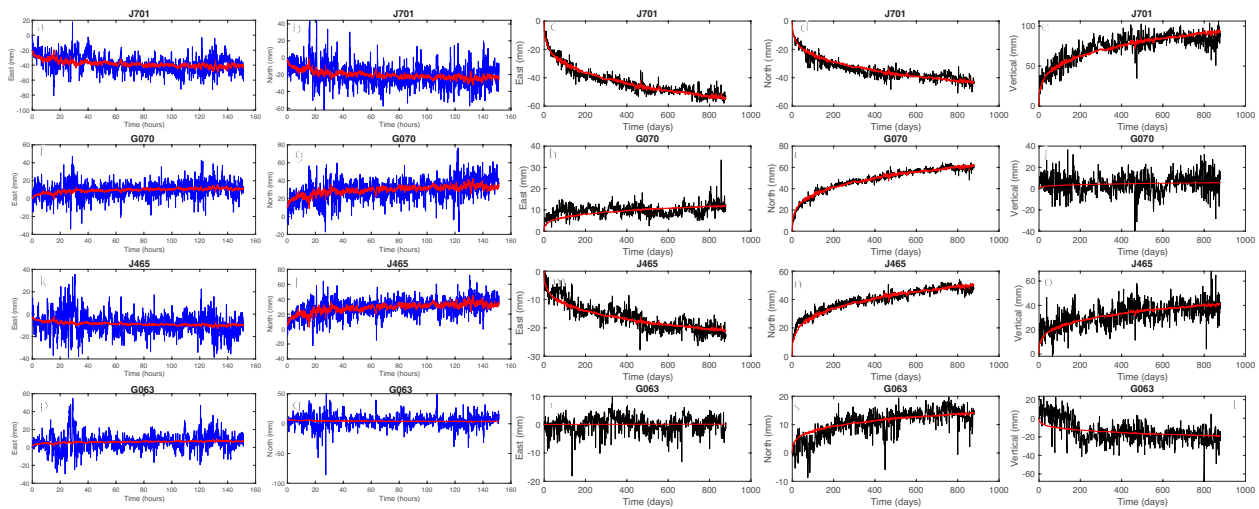
1024

1025

1026

1027

1028



1029

1030 **Fig 6.** GPS time series of four stations (rows), of the five-minute sampled data during the first six
 1031 days (left two columns), and the daily time series during the first two years (right three columns).

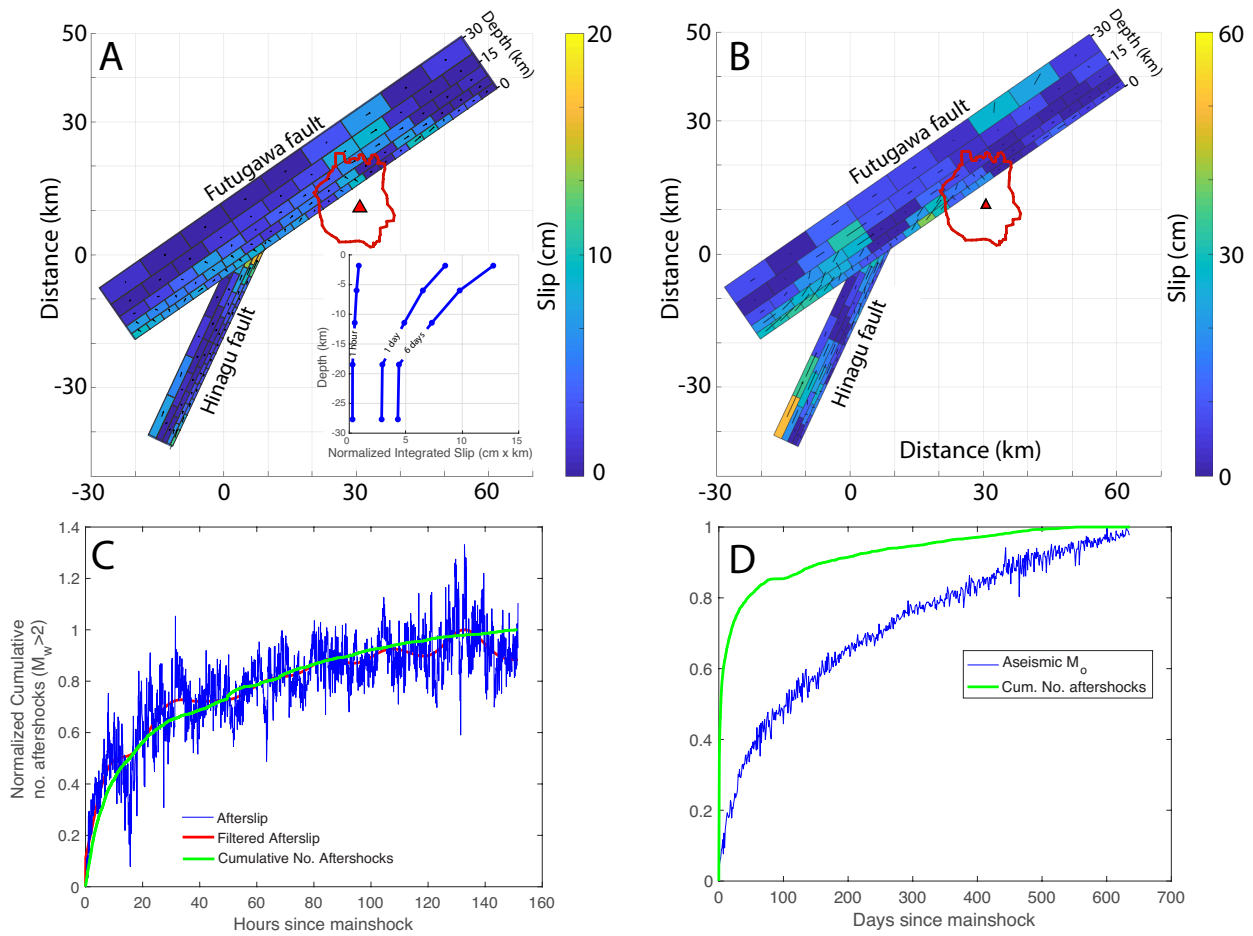
1032 The raw data are shown in blue and black, and the ICA filtered result in red.

1033

1034

1035

1036



1037

1038

1039 **Figure 7. Results of the postseismic slip inversion.** a) and b) show the slip distribution of the

1040 early postseismic phase (after the first day), and longer-term (after the first year), respectively.

1041 Inset in a) shows the evolution of the slip-depth function with time. Comparison of afterslip on a

1042 fault patch (shown in Fig. 8) versus the cumulative number of aftershocks (green lines) for the

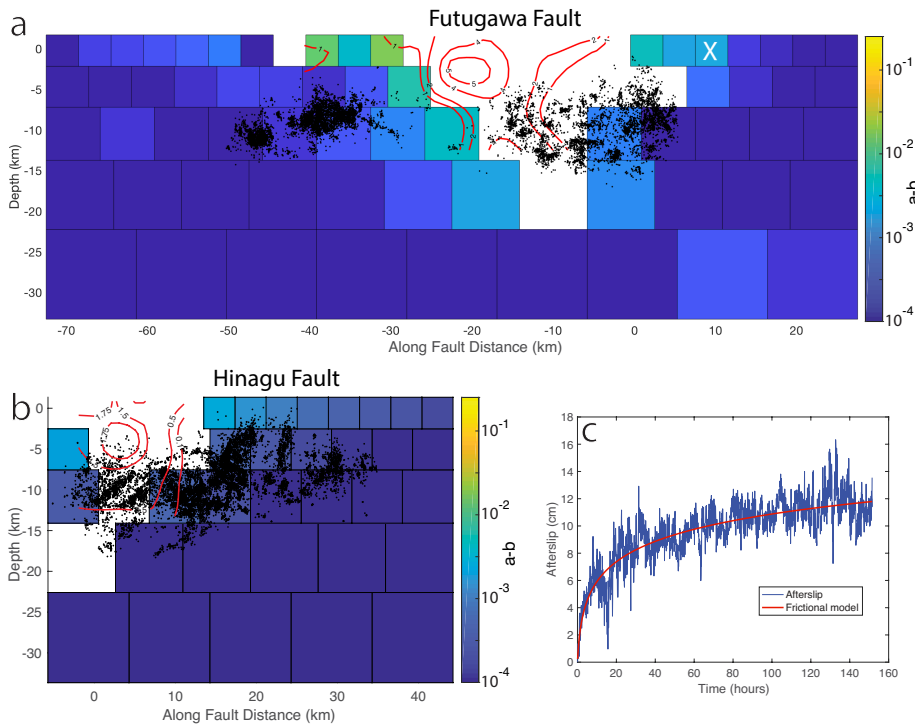
1043 early (first six days) c) and longer-term, first two years d). Early afterslip shows good agreement

1044 with the cumulative aftershocks (with a correlation co-efficient of 0.98), while the longer-term

1045 shows a considerably weaker correlation, likely due to the effect of viscoelastic deformation

1046 biasing our afterslip model.

1047



1048

1049

1050 **Figure 8.** Estimates of frictional $a-b$ values for each fault patch. a) and b) show $a-b$ values for the
 1051 Futugawa and Hinagu faults respectively, blank patches are those that slip coseismically and
 1052 experienced a stress drop, black dots show aftershocks from the template matching catalogue
 1053 within 5 km of the model fault plane, and red contours delineate slip from the coseismic model
 1054 (Figure 5) (Yue et al., 2017). c) shows the fit of the frictional model (red line) from eq. (4), to
 1055 alterslip (blue line) from a single patch, where the location is shown by the white X symbol in (a),
 1056 on the Futugawa fault.

1057

1058

1059

1060

1061

1062

1063

1064

1065

1066